Electromagnetic Modeling of Terahertz Quantum Cascade Laser Waveguides and Resonators

by

Stephen Michael Kohen

B.S., Electrical Engineering (2002)
University of Illinois at Urbana-Champaign

Submitted to the
Department of Electrical Engineering and Computer Science
in partial fulfillment of the requirements for the degree of

Master of Science in Electrical Engineering and Computer Science

at the

MASSACHUSETTS INSTITUTE OF TECHNOLOGY

May 2004

Author .....
Department of Electrical Engineering and Computer Science
May 25, 2004

Certified by ....
Qing Hu
Professor
Thesis Supervisor

Accepted by .....
Arthur C. Smith
Chairman, Department Committee on Graduate Students

Electromagnetic Modeling of Terahertz Quantum Cascade Laser Waveguides and Resonators

by

Stephen Michael Kohen

Submitted to the
Department of Electrical Engineering and Computer Science
on May 25, 2004,
in partial fulfillment of the requirements for the degree of
Master of Science in Electrical Engineering and Computer Science

Abstract

Finite-element numerical modeling and analysis of electromagnetic waveguides and resonators used in terahertz (THz) quantum cascade lasers (QCLs) is presented. Simulations and analysis of two types were performed: two-dimensional waveguides, and two- and three-dimensional resonators. Both metal-metal and semi-insulating (SI) surface-plasmon geometries were investigated. Waveguide simulations extend previous one-dimensional analyses to two dimensions; resonator simulations in two and three dimensions are presented for the first time. The waveguide simulations quantitatively show when two-dimensional effects become non-negligible in their effect on the figure-of-merit relative to previous one-dimensional analyses. The resonator simulations quantitatively show the hybrid optical/microwave nature of THz facet reflectivities, demonstrating that both the effective index method and the impedance mismatch method are poor methods in calculating mirror reflectivities for metal-metal waveguides in the THz region. The effective index method is shown to still be valid for SI surface-plasmon waveguides. In addition, simulated radiation patterns are presented for both waveguiding structures.

Thesis Supervisor: Qing Hu
Title: Professor

Acknowledgments

"For my part, I know nothing with any certainty... but the sight of the stars makes me dream." ~ VvG

To say the very least, I feel extremely honored and privileged to have had the opportunity to join the THz QCL project and experience the excitement that comes with being apart of truly groundbreaking scientific research. I would like to thank my advisor Qing Hu for making this tremendous opportunity possible and for setting a remarkable example in finding joy in the search for understanding.

I would also like to thank my labmates: Ben Williams, Sushil Kumar, and Hans Callebaut. With their hard-working and amiable nature, they have made the lab a fun and enjoyable place to call work. I am especially grateful to Ben Williams for all of the time and patience he has given me in answering all of my questions from waveguides to kernels.

And what would life in Boston have been like without all of the wonderful friends I have met since moving here just under two years ago. To the "phatfriends" group: for keeping things sane with all the fun adventures experienced and yet to come. Special thanks go out to: Tyrone Hill, Shawn Kuo, and Chris Rycroft, the kind of roommates that make what I call home a place I look forward to going back to everyday; Tony Lau, for while setting a remarkable example in the art of procrastination, for also keeping things in perspective for me; Sarah Rodriguez, for spicin' things up with her ever so modest personality; Vikas Anant, for fun times at Tang and lunch breaks at the Whitehead; Kaity Ryan, fellow rower (once-upon-a-time), for making things interesting for us all through her famous seminar series; Amil Patel, for all the afternoon conversations and work breaks; Ming Tang, my solid-state physics buddy and fellow dim sum craver; and of course the ever so vivacious Vivian Lei, for, aside from being punctually late, is as loyal and fun as they come!

Finally, I want to thank my family. To my parents, for the love and support (and patience) they have shown over the years; and to my sister, for her ever continuing support and lasting friendship.

I would also like to acknowledge the financial support of the MIT Presidential Fellowship and of the Department of Defense's National Defense Science and Engineering Fellowship.

Contents

List of Figures

List of Tables

Chapter 1

Introduction

1.1 Project Statement

This master's research project involves the numerical simulation and analysis of electromagnetic waveguides and resonators used in terahertz (THz) quantum cascade lasers (QCLs). Recent research in THz QCLs has shown them to hold considerable potential as a source of coherent THz radiation for bridging the so-called "Terahertz Gap" [1, 2, 3]. The THz frequency range (1–10 THz, 30–300 μm), also known as the far-infrared, has long been identified to have wide-ranging applications in spectroscopy, imaging, and remote sensing. However, due to a lack of compact, cheap, and convenient continuous-wave (CW) THz sources, this frequency range has so far been underdeveloped.

A key development in the extension of QCLs from the mid-infrared regime into longer wavelengths entailed the novel design of confinement structures. This was due, in main, to two parts:

1. Previous conventional dielectric waveguides failed to scale appropriately with wavelength.

2. Free carrier loss increases as the laser frequency approaches the plasma frequency.

The former is a confinement issue while the latter is a loss issue, both important

aspects of waveguide design (refer to Chapter 3). To date, two types of waveguides, both utilizing the surface-plasmon as the confinement mechanism, have enabled CW laser operation: the semi-insulating (SI) surface-plasmon waveguide [4, 5] and the metal-metal waveguide [6].

1.2 Historical Development

This section presents the evolution of surface-plasmon type waveguides from the conventional optical waveguides from which QCLs have slowly been extended into longer and longer wavelengths in the decade since they were realized.

QCLs are based on intersubband emission in a multiple quantum well (MQW) structure. Intersubband emission in a superlattice was first observed at ~ 2.2 THz in 1988 [7], which is well inside the terahertz frequency range. However, QCLs were only first realized in the mid-infrared range in 1994 [8], and were based on conventional dielectric waveguides. One of the main reasons mid-infrared QCLs were developed first, even though efforts proceeded simultaneously with far-infrared QCLs, was due to both the substantial increase in free carrier absorption (Eq. 3.14: $\alpha_w \propto \lambda^2$) in the waveguide and issues with radiation confinement at the longer far-infrared wavelengths. Waveguide design for the original mid-infrared QCLs, operating around 4 μm or 75 THz, was a simple extension of conventional dielectric slab waveguides from optics [8] (see Fig. 1-1(a)). Typical dielectric waveguides provide mode confinement and overlap with the active region by utilizing refractive index contrast between a high index layer sandwiched between cladding layers of lower refractive index. The magnitude of the confinement factor is determined by the ratio of refractive indices and the thickness of the core layer. The key aspect of dielectric waveguides is that propagation characteristics are preserved as the layer thicknesses scale linearly with the effective wavelength of the radiation in those media. Therefore, the preservation of the confinement and propagation characteristics of well-established optical waveguide designs into the mid-infrared required thick layers for efficient confinement [9].

However, two factors arise at infrared wavelengths that make it difficult to main-

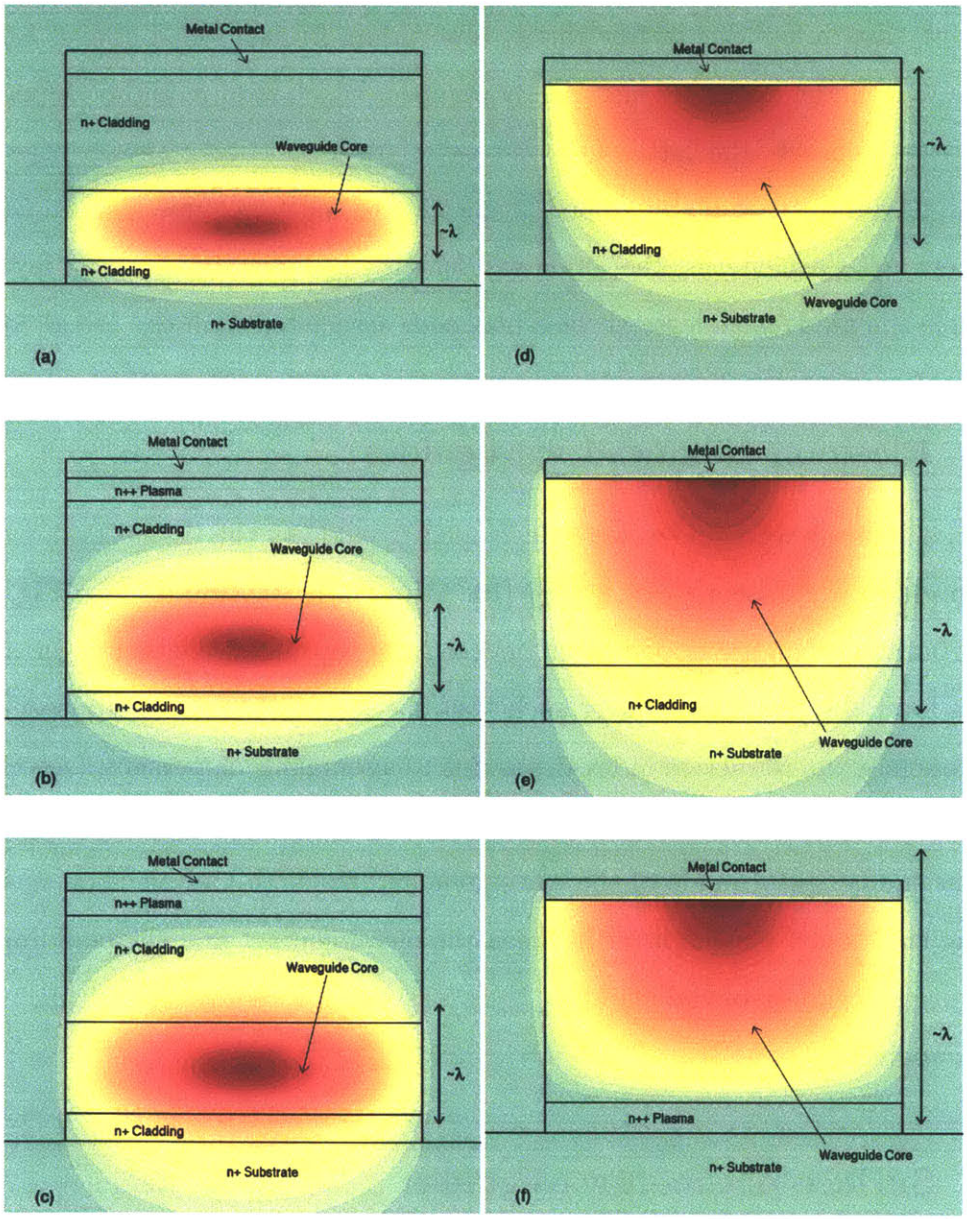

Figure 1-1: Evolution of QCL waveguides: generalized geometries and field profiles of a (a) conventional dielectric waveguide ($\lambda \sim 4$ μm) (b) plasmon-enhanced waveguide ($\lambda \sim 8$ μm) (c) plasmon-enhanced waveguide ($\lambda \sim 12$ μm) (d) single-sided surface-plasmon waveguide ($\lambda \sim 12$ μm) (e) single-sided surface-plasmon waveguide ($\lambda \sim 24$ μm) (f) double-sided surface-plasmon waveguide ($\lambda \sim 24$ μm). (Vertical dimensions are to scale; lateral dimensions are not to scale.)

tain the figure of merit (see Eq. 3.8 in a later section) relative to optical wavelengths: a prohibitive increase required of layer growth by molecular beam epitaxy (MBE), and an increase in loss due to free carrier absorption, as mentioned above. Since the present QCLs under study are electrically pumped, which require highly doped layers for electrical contact, the latter becomes especially important: any leakage of the radiation field into these highly doped layers adds to the waveguide loss. In addition, at long enough wavelengths, the mode will leak further into the cladding layers and can couple the mode with lossy surface-plasmons associated with the metal contacts.

1.2.1 Plasmon-enhanced waveguides

Plasmon-enhanced waveguides were developed to address this issue for long wavelength mid-infrared lasers ($\lambda > 8$ μm) [10, 11]. These waveguides, see Fig. 1-1(b-c), incorporated a highly doped layer between the top metal contact layer and the cladding layer; by doping the layer such that the plasma frequency approaches the laser frequency, the refractive index drops due to anomalous dispersion, (see Eq. 3.13 in a latter section), thereby increasing confinement and suppressing the coupling between the fundamental mode of the waveguide and the high-loss plasmon mode. By including this doped plasma layer between the metal contact and the cladding layer, the required thickness of the cladding layer was thereby reduced to within realistic growth capabilities of MBE.

1.2.2 Surface-plasmon waveguides

An additional waveguide was designed for $\lambda = 8$ and 11.5 μm such that the cladding layer was done away with altogether, see Fig. 1-1(d-e), by depositing a metal contact directly on the active region [9] (the mode still leaks into the substrate). In this case, the interface mode is named a surface plasmon, because the optical response of nearly free electrons is below the frequency of charge-density oscillations, meaning the real part of the metal's dielectric constant is negative. The advantage that this scheme provided was twofold: the required total layer thickness was drastically

reduced (though the active region thickness still scaled on the order of the effective wavelength) and the confinement factor became considerably higher. However, the offset in increased loss due to surface plasmon waves at the metal-semiconductor interface prevented this from being a practical design for mid-infrared QCLs with $\lambda < 15$ μm [12]. The surface-plasmon, due to its strong coupling capabilities, also presents itself as a prime method for constructing a distributed feedback mechanism. Tredicucci was able to extend the concept of distributed feedback (DFB) lasers to such surface-plasmon lasers by utilizing a two-metal grating [12]. The single-sided surface-plasmon waveguide has been used to make QCLs at $\lambda = 17$ μm [12], $\lambda = 19$ μm [13], and $\lambda = 21.5$ and 24 μm [14]. Ref. [14] also reported the first THz QCL to utilize a double-sided surface-plasmon waveguide at $\lambda = 21.5$ μm. In this case, a 750-nm-thick heavily doped layer, see Fig. 1-1(f), was included between the active region and the substrate. Though the confinement factor increased to $\Gamma \sim 0.98$, this was offset by an increase in free carrier absorption from the heavily doped layer. Nevertheless, it was concluded that the design was still a viable option for far-infrared QCLs on the lower-energy side of the *Reststrahlen* band ($\lambda > 50$ μm), where the lower frequencies would be further from the plasma frequency of the doped layers, and thus a lower loss would result. This design of a double-sided surface-plasmon was taken one step further by making a double metal-semiconductor waveguide for QCLs with wavelengths of 19, 21, and 24 μm [15]. Xu had earlier worked on metal-metal waveguide fabrication and modeling for THz QCLs [16]. This type of waveguide ultimately led to the metal-metal waveguides used in THz QCLs today. However, the fabrication complexity for this type of structure led to its later development after the SI surface-plasmon waveguide had already been shown to make THz QCLs feasible.

1.2.3 Semi-insulating surface-plasmon waveguide

It was finally a breakthrough in the waveguide design that helped lead Köhler *et al.* in 2001 to demonstrate the first terahertz QCL at 4.4 THz [1]. Their waveguide, shown in Fig. 1-2, was based on the previously developed double-sided surface-plasmon, with the exception that they used a semi-insulating substrate to reduce any modal overlap

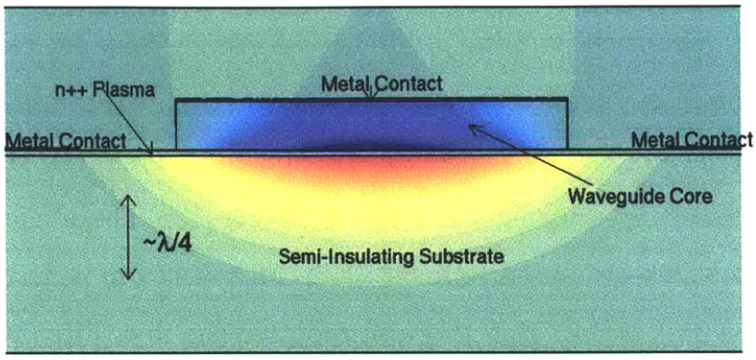

Figure 1-2: General geometry and field profile of a semi-insulating surface-plasmon waveguide ($\lambda \sim 68$ μm).

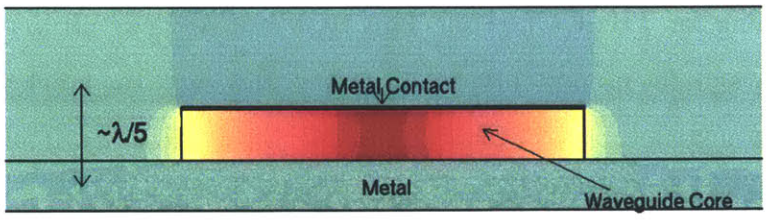

Figure 1-3: General geometry and field profile of a metal-metal waveguide ($\lambda \sim$ 100 μm).

with doped regions; this prevented a prohibitive increase in free carrier absorption from taking place at the far-infrared wavelengths in comparison with the mid-infrared wavelengths. The structure, termed semi-insulating surface-plasmon, made possible a mode composed of a surface plasmon bound to the upper metallic contact and to the lower heavily doped layer. Surface-plasmons are discussed in more detail in Appendix B. Electrical contact is made possible by side metal contacts on top of the heavily doped layer.

1.2.4 Metal-metal waveguide

The next major breakthrough in waveguide design came when Williams *et al.* in 2003 demonstrated the first terahertz QCL at 3.0 THz using a metal-semiconductor-metal waveguide for confinement [17], see Fig. 1-3. This waveguide design eliminated any free carrier loss associated with the heavily doped plasma layers while providing high confinement, $\Gamma \sim 1$, which becomes advantageous at even longer wavelengths. In addition, the contribution by the surface plasmons to the waveguide loss decreases with increasing wavelength as the frequency deviates further from the surface plasma frequency. The predominant loss mechanism at these wavelengths, therefore, becomes free carrier absorption with carriers in the active region itself.

1.3 Motivation for Simulations

Up to this point, previous design simulations were all performed in one dimension and based on a slab waveguide technique [18]. However, it becomes unclear how much of an effect certain two dimensional parameters have on the final figure of merit. Specifically, the effects of the width of the waveguide, which can easily be made less than the effective wavelength, and the effects of the metal contact gap distance [19] need to be quantified and analyzed. The effects of varying substrate thicknesses for SI surface-plasmon waveguides and waveguide core thicknesses for metal-metal waveguides also need to be known.

In addition, previous design simulations calculated mirror loss using the effective-

index method. For an GaAs/Air interface, this turns out to give a facet reflectivity of $R \sim 0.32$. In this case, mirror loss, given by Eq. 3.9, $\alpha_m = -\ln R/L$, where L is the cavity length, is solely a function of the cavity length [1, 20, 21]. This made sense from the perspective that QC laser resonator design had evolved from optical resonator design, where the reflection coefficient is simply the Fresnel reflection coefficient [22], which is determined solely by the effective mode index. Though this still works fine for mid-infrared QC lasers [8, 23], at longer wavelengths beyond the far-infrared and in the microwave regime, waveguides are designed using transmission line theory. In this regime, reflectivities are solved by using the impedance mismatch method. In the present context, THz waveguides are hypothesized to be a hybrid of conventional optical and microwave waveguides. Numerical computations were carried out for this thesis to offer a numerical solution to the problem of determining THz facet reflectivities. Resonator simulations for metal-metal waveguides in two and three dimensions and for SI surface-plasmon waveguides in two dimensions are analyzed for the first time.

1.4 FEMLAB - Simulation Method

The numerical modeling and simulations in this thesis were carried out for all two- and three-dimensional problems in a commercial finite-element based partial differential equation software package called FEMLAB, which is also capable of post-processing interaction with MATLAB. One dimensional simulations were carried out in MATLAB using the previously mentioned numerical program in Ref. [18]. FEMLAB provides a powerful environment in solving complicated differential equations. The main attractions of FEMLAB were twofold: its inherent ability to model complex geometries using the finite element method and the addition of an electromagnetics module with numerous predefined modes of electromagnetism (electrostatics, quasi-statics, and waves in 1D, 2D, and 3D), described in Appendix A. Waveguide simulations are solved in the perpendicular-plane eigenmode solver, while resonator simulations are solved in the two-dimensional in-plane and three-dimensional full-wave linear station-

ary mode solvers.

1.5 Thesis Overview

This thesis presents numerical results in the design of terahertz quantum cascade laser resonators. Chapter 2 provides a brief overview of the theory behind the numerical method used by FEMLAB: the finite element method. Chapter 3 describes the issues in the design of terahertz quantum cascade laser resonators and waveguides. Chapter 4 presents results of waveguides simulations. Chapter 5 presents results of resonator simulations.

Chapter 2

Brief Overview of the Finite Element Method

2.1 Introduction

The finite element method (FEM) was first proposed in the 1940s [24] and saw its first application in aircraft design in the 1950s. Its first application to electromagnetic problems was not realized until the late 1960s; however, today it is widely used in a large variety of electromagnetic problems. Since its early days, the FEM has evolved into a well-developed numerical technique [25, 26, 27, 28] for obtaining approximate solutions to boundary-value problems. As the name suggests, the basic premise behind this technique is the discretization of the solution domain into a finite number of subdomains (elements), on which the solution is approximated by a piecewise interpolation function.

In order to see the usefulness and effectiveness of the FEM it is instructive to compare it with the finite difference method (FDM), which is the other most widely used method for solving boundary-value problems. Both methods attempt to approximate the solution to a given boundary-value problem by first discretizing the solution domain. While the FDM gives a point-wise approximation to the governing equations, the FEM gives a piecewise approximation, thereby specifically assigning a solution everywhere in the solution domain rather than just on a grid of points. In

the actual approximation of the geometry in the problem, the FDM creates a grid of arbitrarily spaced points, whereas the geometry in the FEM creates an arbitrary collection of arbitrarily shaped elements (usually triangles), thereby making the method much more well suited for geometries having greater complexity. In addition, difficulties can be encountered with the FDM in cases where complex boundary conditions are required; the FEM has greater flexibility in handling boundary conditions. Especially important is the attention that must be paid to the amount of computer power needed to formulate and assemble the problem in addition to solving the problem. In this respect, the FEM usually supersedes the FDM for problems in two or more dimensions.

In this chapter, the fundamental principles and procedures underlying the FEM are briefly presented. The treatment is standard and is based on that in Jin [26]. For further details, please refer to the References [25, 27, 28].

2.2 Classical Methods for the Approximate Solution of Boundary-Value Problems

Linear boundary-value problems are generally defined by a governing differential equation in the operational form

$$\hat{L}u = f, \tag{2.1}$$

on the domain Ω, where $\hat{L}$ is a differential operator, f is a source or force function, u is unknown, and where boundary conditions on the boundary $\partial\Omega$ must also be defined. Boundary conditions range from Dirichlet ($u = u_0$) and Neumann ($\nabla u = u_0'$) conditions, where u_0 and u_0' are constants, to more complicated matched-boundary and absorbing conditions.

For most real-world problems, the domain Ω is complicated enough to prevent an analytical solution to Eq. (2.1). Among the most widely used approximation methods are the Rayleigh-Ritz and Galerkin methods described below, which form the basis for the FEM.

2.2.1 The Rayleigh-Ritz method

The Rayleigh-Ritz method, also known as the Ritz method, reformulates the original differential equation boundary-value problem, Eq. (2.1), as a variational problem. As a variational problem, the calculus of variations is used to find the minimum or maximum of a given functional; this extremum corresponds to the solution to the differential equation. An approximate solution to this variational problem can be found by setting up a solution with respect to a number of variable parameters that define the approximation; therefore, minimization of the functional with respect to these variables gives the best approximation. This problem is the opposite of that encountered in most applications using the calculus of variations, which is: given some minimization principle, such as Hamilton's Principle in physics, what is the governing differential equation. Here we are searching for the functional given the differential equation.

This problem can be illustrated for the simplest case in which the operator $\hat{L}$ is self-adjoint and positive definite, as defined below, and is referred to as the standard variational principle. If we define an inner product by

$$\langle u|v\rangle \equiv \int_{\Omega} u^* v \; d\Omega, \tag{2.2}$$

then an operator is self-adjoint if

$$\langle \hat{L}u|v\rangle = \langle u|\hat{L}v\rangle,$$

and positive definite if

$$\langle \hat{L}u|u\rangle = \begin{cases} > 0 & u \neq 0 \\ = 0 & u = 0. \end{cases}$$

In such a case, the solution to Eq. (2.1) can be found by minimizing the functional given by

$$I(u) = \frac{1}{2}\langle \hat{L}u|u\rangle - \frac{1}{2}\langle u|f\rangle - \frac{1}{2}\langle f|u\rangle. \tag{2.3}$$

Proof of this statement follows in two steps: first, it must be shown that the differ-

ential equation (2.1) is a necessary consequence when $I(u)$ is stationary (either at a maximum or minimum), and two, that the stationary point is a minimum.

Taking the first variation of Eq. (2.3), we have

$$\delta I = I(u+\delta u) - I(u) = \frac{1}{2}\langle \hat{L}\delta u|u\rangle + \frac{1}{2}\langle \hat{L}u|\delta u\rangle - \frac{1}{2}\langle \delta u|f\rangle - \frac{1}{2}\langle f|\delta u\rangle.$$

Employing the self-adjoint property on the first term, we have

$$\begin{aligned}
\delta I &= \frac{1}{2}\langle \delta u|\hat{L}u\rangle + \frac{1}{2}\langle \hat{L}u|\delta u\rangle - \frac{1}{2}\langle \delta u|f\rangle - \frac{1}{2}\langle f|\delta u\rangle \\
&= \frac{1}{2}\langle \delta u|\hat{L}u - f\rangle + \frac{1}{2}\langle \hat{L}u - f|\delta u\rangle \\
&= \frac{1}{2}\langle \delta u|\hat{L}u - f\rangle + \frac{1}{2}\langle \delta u|\hat{L}u - f\rangle^* \\
&= \mathrm{Re}\left\{\langle \delta u|\hat{L}u - f\rangle\right\},
\end{aligned}$$

where the third step follows from the definition of the inner product. Therefore, imposing the stationary requirement $\delta I = 0$ and using the fact that δu is arbitrary, we see that u must be the solution to Eq. (2.1). Taking the second variation of Eq. (2.3) we have

$$\delta(\delta I) = \delta I(u+\delta u) - \delta I(u) = \mathrm{Re}\left\{\langle \delta u|\hat{L}\delta u\rangle\right\}.$$

By imposing the restriction that $\hat{L}$ is positive definite, the above shows that $\delta(\delta I) > 0$ for arbitrary δu. This means that the stationary point is a minimum.

Once the functional given by Eq. (2.3) is determined, an approximate solution is developed using a finite basis trial expansion

$$u_t = \sum_{j=1}^{N} c_j \phi_j = \bar{c}\cdot\bar{\phi} = \bar{\phi}\cdot\bar{c}, \tag{2.4}$$

where ϕ_j are a finite set of expansion functions defined over Ω and c_j are the coeffi-

cients to be determined. Eq. (2.3) becomes

$$I(u_t) = \frac{1}{2}\bar{c} \cdot \langle \hat{L}\bar{\phi}|\bar{\phi}\rangle \cdot \bar{c} - \frac{1}{2}\bar{c} \cdot \langle \bar{\phi}|f\rangle - \frac{1}{2}\langle f|\bar{\phi}\rangle \cdot \bar{c}.$$

The next step is minimization of $I(u_t)$ with respect to the coefficients c_j. This is simple to carry out if the problem is real, and is what follows. In the case the problem is complex, the final result still holds, however its derivation follows differently and may be found in Appendix B of reference [26]. When the problem is real, the partial derivatives are forced to zero and the following set of linear equations are constructed

$$\begin{aligned}
\frac{\partial}{\partial c_i} I(u_t) &= \frac{1}{2}\langle \hat{L}\phi_i|\bar{\phi}\rangle \cdot \bar{c} + \frac{1}{2}\bar{c} \cdot \langle \hat{L}\bar{\phi}|\phi_i\rangle - \langle \phi_i|f\rangle \\
&= \frac{1}{2}\left(\langle \hat{L}\phi_i|\bar{\phi}\rangle + \langle \hat{L}\bar{\phi}|\phi_i\rangle\right) \cdot \bar{c} - \langle \phi_i|f\rangle = 0 \\
&= \langle \phi_i|\hat{L}\bar{\phi}\rangle \cdot \bar{c} - \langle \phi_i|f\rangle = 0,
\end{aligned}$$

for $i = 1, 2, \ldots, N$, and where the last step follows because $\hat{L}$ is self-adjoint and the problem is real. This can be written as the matrix equation

$$A\mathbf{x} = \mathbf{b}, \tag{2.5}$$

where

$$A_{ij} = \langle \phi_i|\hat{L}\phi_j\rangle, \qquad b_i = \langle \phi_i|f\rangle,$$

and where $\mathbf{x} = \mathbf{c}$ are the coefficients to be determined. By the self-adjoint property of $\hat{L}$ it is also seen that A is a symmetric matrix ($A_{ij} = A_{ji}$). Therefore, the approximate solution for Eq. (2.1) is obtained by solving for the finite basis coefficients in the above matrix equation.

Limitations of the standard variational principle

Since the standard variational principle requires a self-adjoint operator $\hat{L}$, it is limited to cases involving lossless media and homogeneous boundary conditions. The latter limitation may be removed by using a modified variational principle, which is beyond

the scope of this overview [26], and can be employed in almost all electromagnetic problems involving lossless media. In the case that the problem involves lossy media, the associated operators are complex; the definition of the inner product, Eq. 2.2, directly limits the standard variational principle to real operators. If a new inner product is defined by

$$\langle u|v\rangle \equiv \int_{\Omega} uv \; d\Omega, \tag{2.6}$$

then this limitation is removed. The inner product defined by Eq. 2.2 is referred to as the inner product in Hilbert space, whereas the one defined in Eq. 2.6 is referred to as the symmetric product. Therefore, the question of whether an operator is self-adjoint depends on the definition of the inner product. It can be shown that with this new definition for the inner product, Eq. 2.3 remains valid and is referred to as the generalized variational principle.

2.2.2 The Galerkin method

It is evident that the Rayleigh-Ritz method rests on if the differential equation operator $\hat{L}$ is capable of being formulated as self-adjoint. In the case it is not, Galerkin's method is often used. Galerkin's method is a special case of the weighted residual method. The method is based on weighting the residual of the differential equation. If we have an approximate solution, u_t, the residual is defined as following

$$r \equiv \hat{L}u_t - f,$$

which is not equal to zero for the approximate solution u_t. By forcing the weighted residuals, defined below, to be zero on Ω gives the best approximation:

$$R_i \equiv \int_{\Omega} w_i r \; d\Omega = 0,$$

where the w_i are a given set of weighting functions. Galerkin's method employs as the weighting functions the same as those used for the expansion of the trial solution,

Eq. (2.4): $w_i = \phi_i$. The weighted residual integrals become

$$R_i = \int_\Omega \left(\phi_i \hat{L} \bar{\phi} \cdot \bar{c} - \phi_i f \right) d\Omega.$$

Analogous to Eq. (2.5), this results in a matrix system for the coefficients $\bar{c}$. If the operator $\hat{L}$ is self-adjoint, the matrix system produced by Galerkin's method will reduce to the same matrix system produced by the Rayleigh-Ritz method. It should be added that a variety of other residual methods exist that employ different sets of weighting functions.

2.3 The Finite Element Method

The Rayleigh-Ritz and Galerkin methods described above expand approximate solutions to Eq. (2.1) using a finite basis set of functions defined over all of Ω, Eq. (2.4). For problems in more than one dimension, it is usually a nontrivial matter in defining these basis functions. The FEM approaches this problem by dividing the domain Ω into many subdomains; by making the subdomains small enough such that the solution does not vary in any complicated way, a trial function can be constructed from a linear combination of simple approximate solutions on each subdomain. Once these functions have been defined, either the Rayleigh-Ritz method or Galerkin method may be used to solve the problem. The former is known as the variational finite element method and the latter as the Galerkin finite element method.

Thus, the finite element method is based on dividing the domain into subdomains and constructing a trial solution composed of a linear combination of basis functions defined over each respective subdomain. This differs from the classical Rayleigh-Ritz and Galerkin methods in that they construct a trial solution composed of a linear combination of basis functions defined over the whole domain.

2.3.1 Basic procedure

While there exist numerous cases that each approach setting up the FEM differently, all FEM problems follow the four basic steps: discretization, determination of appropriate interpolation functions, setting up the system of equations, and finally solving these equations. FEMLAB uses a meshing algorithm to discretize the domain into triangular subdomains in two dimensions, and tetrahedra in three dimensions. Fig. 2-1(a) shows a sample triangular discretization. One major advantage of the FEM is that it allows one to arbitrarily fine tune a mesh, such that there is more resolution in areas of the geometry you feel there might be important variations in the solution. This factor was indispensable in the simulations presented in this thesis, as the aspect ratios of various geometries would have made a uniform mesh impractical to implement. Other options in the discretization step for the FEM, though not implemented by FEMLAB, include rectangular discretization for two dimensions and triangular prisms or cuboids for three dimensions. In selecting the interpolation functions, FEMLAB has default cases optimized for each application mode. These include first, second, and higher-order polynomials in some two-dimensional cases and linear vector elements for two- and three-dimensional cases. Linear vector elements are necessary in certain electromagnetic applications modes in order to make the boundary conditions between subdomains self-consistent with Maxwell's equations. Fig. 2-1(b) shows a linear interpolation function on one triangular element in which the function is approximated as $u(x, y) = a+bx+cy$, where a, b, and c are the variable parameters. The final two steps of the FEM, formulating and solving the systems of equations, are both handled by numerous sub-algorithms within the FEMLAB program and are explained in more detail in Ref. [29].

Appendix A discusses in more depth how FEMLAB formulates the setup of partial differential equations. Specifically, the differential equations and boundary conditions for the various electromagnetic mode solvers used in this thesis are discussed.

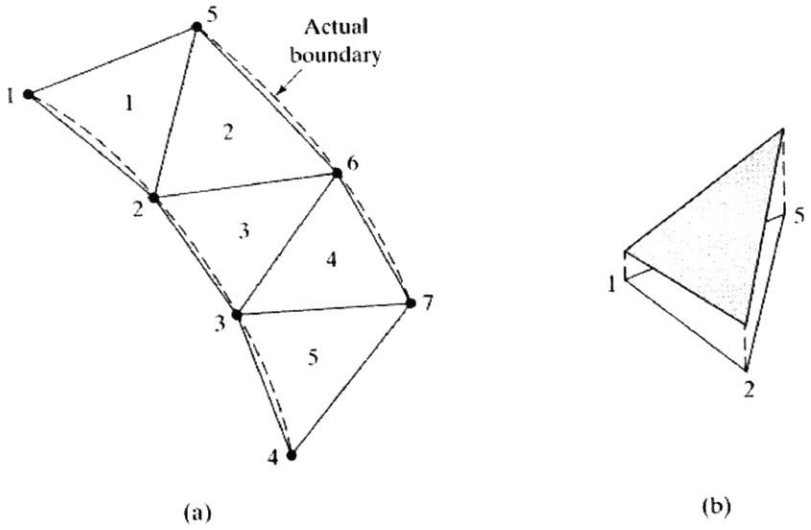

Figure 2-1: FEM example from Ref. [30]: (a) discretization of a region into triangular finite elements, (b) linear variation of trial solution within a triangular finite element.

Chapter 3

Terahertz Quantum Cascade Laser Resonator Theory

3.1 Introduction

The design of terahertz quantum cascade lasers can be fairly independently broken up into the two fundamental components of the laser: design of the gain medium and design of the resonator. The gain medium for THz QCLs consists of stacked layers (on the order of 1000) of quantum wells designed such that lasing occurs on selected intersubband transitions in the conduction band of a semiconductor heterostructure. A variety of designs have successfully been implemented, including the chirped superlattice design [1, 2], the resonant-phonon design [3], and the bound-to-continuum design [5]. Aside from some minor dependent parameters, such as doping levels and the average permittivity in the active region, the only important factor to take away from any of the gain medium designs for the purpose of resonator design is the desired lasing frequency.

This chapter deals with the resonator, which in turn can be broken up into two main components: a waveguide and mirrors. The waveguide is necessary in order to confine the radiation to the gain medium in order for the fields to be amplified. The mirrors are necessary in order to provide optical feedback. In addition, the waveguide and mirrors contribute losses given as α_w (absorptive) and α_m (coupling),

respectively. Waveguide losses are due to the intrinsic electromagnetic properties of the materials used. Mirror losses are due to the finite mirror reflectivities, R, and provide the output coupling mechanism for the laser.

3.2 Threshold Condition for Laser Oscillation

The necessary condition for a particular mode of a waveguide to lase is that the wave reproduce itself after one round-trip. Let a particular mode traveling in the z direction be represented by a spatial field profile $\mathbf{h}(x, y)$ and have a propagation constant β, which may be written as

$$\beta = \beta' + i\beta''. \tag{3.1}$$

Assuming time dependence $\sim e^{-i\omega t}$, the full field is $\mathbf{H}(x, y, z) = \mathbf{h}(x, y)e^{i\beta z}$. The imaginary part of the propagation constant, β'', can be decomposed into gain and lossy components

$$2\beta'' = \alpha_w - g_{\text{modal}}, \tag{3.2}$$

where α_w includes all absorptive losses contributed by the waveguide, and g_{modal} is the power gain experienced by the mode. Simple approximate methods [22] give the relationship between the modal gain and the active material gain, g, as

$$g_{\text{modal}} = \Gamma g, \tag{3.3}$$

where Γ is called the confinement factor and is defined as the fraction of power guided in the active region:

$$\Gamma = \frac{\frac{1}{2}\iint_{\text{inside}} \text{Re}\{\mathbf{e} \times \mathbf{h}^*\}\, dxdy}{\frac{1}{2}\iint_{\text{total}} \text{Re}\{\mathbf{e} \times \mathbf{h}^*\}\, dxdy}. \tag{3.4}$$

g is the material gain that only depends on the gain medium.

The round-trip condition can be written, assuming a cavity bounded by identical

mirrors, as

$$|r|^2 e^{i2\phi_r} e^{i2\beta L} = 1, \tag{3.5}$$

where L is the length of the cavity, and $r = |r|e^{i\phi_r}$ is the reflection coefficient for one facet. Equating the phases of Eq. 3.5 gives the Fabry-Pérot resonance condition:

$$\beta' L = m\pi - \phi_r \quad \text{for any integer } m. \tag{3.6}$$

For most cases, ϕ_r is generally negligible and can be neglected. Equating the amplitudes of Eq. 3.5, where the mirror reflectivity is $R = |r|^2$, gives

$$\beta'' = \frac{1}{L} \ln |r| = \frac{1}{2L} \ln R. \tag{3.7}$$

From Eqs. 3.2, 3.3, and 3.7, the gain threshold condition can be written as

$$g_{\text{th}} = \frac{1}{\Gamma} \left(\alpha_w - \frac{1}{L} \ln R \right) = \frac{\alpha_w + \alpha_m}{\Gamma}. \tag{3.8}$$

Here, the mirror coupling loss is:

$$\alpha_m = -\frac{1}{L} \ln R. \tag{3.9}$$

In Eq. 3.8, g_{th} represents the value that the small-signal gain coefficient of the gain medium must reach in order for lasing to occur. This important parameter is usually referred to as the figure-of-merit in the resonator design of lasers and plays a critical role in the final performance of the laser; attention must be paid to the particular variable parameters if one seeks the optimal performance.

3.3 Loss Mechanisms

The total loss that the modal gain must reach to achieve lasing comes from waveguide and mirror contributions. The predominant waveguide loss mechanisms in the THz regime comes from free carrier absorption and phonon absorption. Absorptive waveg-

uide losses should obviously be kept at a minimum in order to keep the threshold gain condition as low as possible. On the other hand, the contributions from the mirror losses need not necessarily be made as small as possible, because they also function as the output coupling mechanism for the laser. Mirror facet issues in the THz regime will be discussed at the end of this Chapter.

3.3.1 Free carrier absorption loss

Free carrier effects are modeled within FEMLAB by including their contributions to the complex permittivities. Classical Drude theory for conductivity presents the simplest theory for modeling these effects and is described in Ref. [31]. The basic approximation behind this theory assumes a classical gas of electrons with a mean free time between collisions of τ, known as the relaxation time and is obtainable from empirical mobility data. In addition, the theory assumes no spatial variation of the fields, which is a good approximation if the length over which the field varies appreciably is greater than the electron mean free path.

Assuming a driving field $\mathbf{E}(t) = \mathrm{Re}\{\mathbf{E}(\omega)e^{-i\omega t}\}$, the frequency-dependent conductivity, $\sigma(\omega)$, may be defined by the relation $\mathbf{J}(\omega) = \sigma(\omega)\mathbf{E}(\omega)$. The Drude-Lorentz model gives a frequency dependent conductivity

$$\sigma(\omega) = \frac{n_{3D}e^2\tau}{m^*(1 - i\omega\tau)}, \tag{3.10}$$

where n_{3D} is the free carrier density, e is the carrier charge, and m^* is the effective carrier mass. Likewise, a frequency-dependent permittivity, $\epsilon(\omega)$, may be defined by the relation $\mathbf{D}(\omega) = \epsilon(\omega)\mathbf{E}(\omega)$. The conductivity of a material may be included in the permittivity by defining an effective complex dielectric constant given by

$$\epsilon_{\mathrm{Drude}}(\omega) = \epsilon(\omega) - \frac{\sigma(\omega)}{i\omega}. \tag{3.11}$$

All other contributions to the dielectric constant, including phonon effects discussed below, are given in terms of the core dielectric constant $\epsilon(\omega)$, also written as ϵ_{core}. It

is useful to define the plasma frequency

$$\omega_p \equiv \sqrt{\frac{n_{3D}e^2}{\epsilon'_{\text{core}}m^*}}, \tag{3.12}$$

where $\epsilon'_{\text{core}} = \text{Re}\{\epsilon_{\text{core}}\}$. For $\omega > \omega_p$ the material behaves as a dielectric, while for $\omega < \omega_p$ the material behaves as a plasma.

In our gain medium, $\omega_p/2\pi < 1$ THz while $\omega/2\pi > 1$ THz. Thus, to the first order of $\omega_p^2\tau/\omega(1 - i\omega\tau)$, whose amplitude is smaller than unity, the refractive index n becomes

$$n = \text{Re}\left\{\sqrt{\frac{\epsilon_{\text{Drude}}}{\epsilon_0}}\right\} = \sqrt{\frac{\epsilon'_{\text{core}}}{\epsilon_0}}\left(1 - \frac{\omega_p^2\tau^2}{2(1+(\omega\tau)^2)}\right), \tag{3.13}$$

and it can be seen that the refractive index for a dielectric is reduced by anomalous dispersion as the frequency approaches the plasma frequency. To the first order of $\omega_p^2\tau/\omega(1 - i\omega\tau)$, the bulk free carrier loss contribution is

$$\alpha_{\text{fc}} = \sqrt{\frac{\epsilon'_{\text{core}}}{\epsilon_0}}\frac{\omega_p^2\tau}{c(1+(\omega\tau)^2)}. \tag{3.14}$$

For $\omega\tau \gg 1$, which is the case in our gain medium and frequency of interest where $\tau = 0.5$ ps and $f > 1$ THz, the free carrier loss is proportional to λ^2/τ. This is the well-known ω^{-2} dependence of the free carrier absorption loss and is shown in Fig. 3-1.

The scattering times used in the simulations presented in this thesis use those in Table 3.1, which are generally accepted to be valid at temperatures of 77 K [32, 33, 34, 31]. Deviations relevant to the approximations made in the Drude model are discussed in more depth in Ref. [20].

3.3.2 Phonon absorption loss

Optical phonon coupling provides a natural boundary between THz and mid-infrared QCLs; in the vicinity of the *Reststrahlen* band (8-9 THz in GaAs), this coupling causes dispersion and loss for the propagating mode. Moore *et al.* modeled the

Table 3.1: Scattering times, densities, effective masses, and core permittivities used in THz numerical simulations. Bulk plasma frequencies are also noted.

Material	τ (ps)	n (cm^{-3})	m^* (m_e)	ϵ_{core}	$\omega_p/2\pi$ (THz)
GaAs (highly doped)	0.1	1–5$\times 10^{18}$	0.067	12.96	9.64–21.5
GaAs (lightly doped)	0.5	2×10^{15}	0.067	12.96	0.430
Au	0.06	5.9×10^{22}	1	1	2181

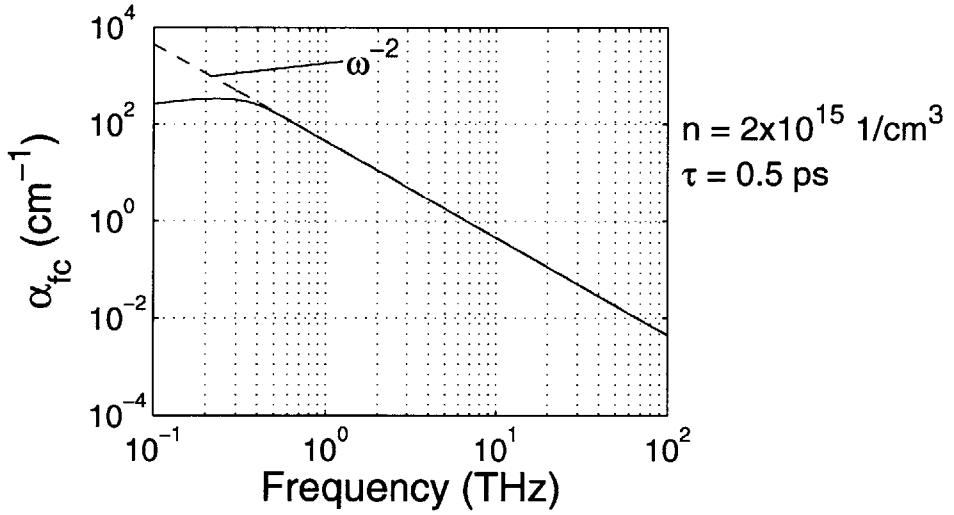

Figure 3-1: Bulk free carrier absorption loss for lightly doped GaAs. The doping is 2×10^{15} cm^{-3} and the scattering time is 0.5 ps.

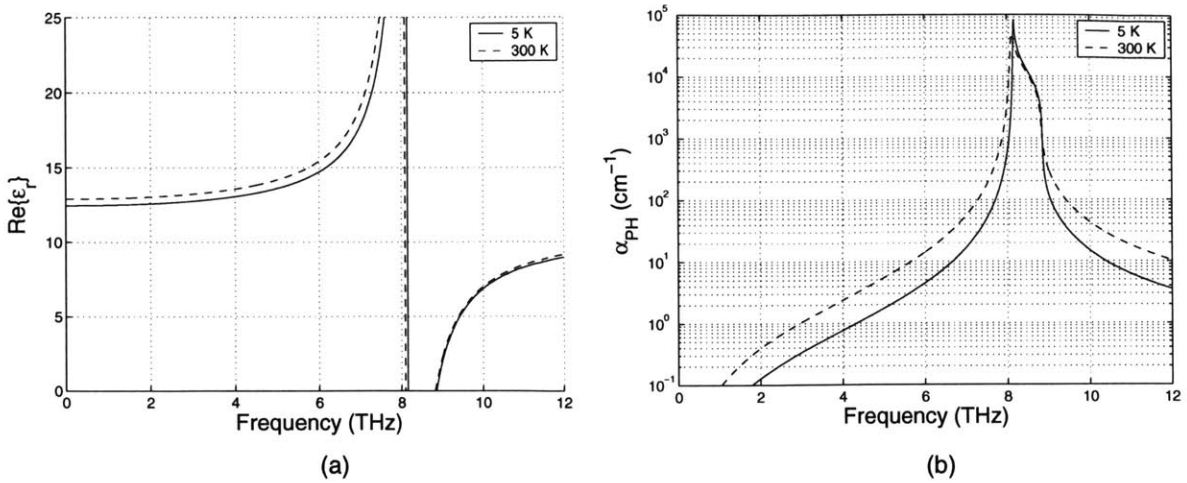

Figure 3-2: Phonon coupling effects in GaAs for $T = 5$ and 300 K: (a) real part of the relative permittivity, (b) the loss.

Table 3.2: Phonon loss values, α_{ph}, calculated from Ref. [35] for $T = 5$, 300 K at selected frequencies.

Frequency (THz)	α_{ph} at 5 K (cm^{-1})	α_{ph} at 300 K (cm^{-1})
2.0	0.1271	0.3936
3.0	0.3356	1.0414
4.0	0.7643	2.3817
5.0	1.7329	5.4385
5.5	2.7050	8.5380
6.0	4.4454	14.152
6.5	7.9713	25.728
7.0	16.728	55.406

permittivity and loss of semi-insulating GaAs in the infrared by fitting experimental data at 5 and 300 K to a two-oscillator model [35] (see Fig. 3-2). This two-oscillator model includes an oscillator for the fundamental optical phonon absorption and an oscillator for near-infrared and visible absorption processes (above 4000 cm^{-1}). For simulations presented in this thesis, the effects of phonon coupling are not included in the core permittivities used for GaAs (see Table 3.1). Since the modal fields of the waveguides considered are contained almost entirely within GaAs, phonon effects may simply be included by adding the respective phonon loss (see Table 3.2 for selected tabulated values) to the calculated waveguide loss: $\alpha_w = \alpha_{\text{fc}}(\text{from simulations}) + \alpha_{\text{ph}}$.

3.3.3 Facet coupling loss

Facets for THz QCLs are created by cleaving the semiconductor along a particular lattice plane; the resulting interface is a relatively perfect plane. From Eq. 3.9, calculation of the facet loss is equivalent to the calculation of the reflection and transmission coefficients of the laser mode at this interface.

Effective index method

In the regime of optics, the laser mode is considered, to a good approximation, to be an infinite plane-wave and the reflection coefficient is simply given by the Fresnel reflection coefficient, which is determined solely by the effective mode index:

$$r_{\text{Fresnel}} = \frac{n_{\text{eff}} - 1}{n_{\text{eff}} + 1}, \tag{3.15}$$

where $n_{\text{eff}} = \beta'/\beta_0 = c\beta'/\omega$ is the effective mode index. Eq. 3.15 is the effective index method, and has been used to calculate mirror reflectivities for mid-infrared QCLs [8] and SI surface-plasmon THz QCLs [1, 3, 21]. For an GaAs/Air interface, $R \sim 0.32$. Chapter 5 presents results that suggest this method does hold true in the calculation of SI surface-plasmon reflectivities.

Impedance mismatch method

The infinite plane-wave approximation begins to break down once the size of the guiding structure becomes on the order of the wavelength; this certainly holds true for metal-metal waveguides, similar to micro-strip transmission lines, where aperture sizes are much less than the free-space wavelength, $d \ll \lambda_0$. The impedance mismatch method from transmission line theory [36] becomes suitable for a description in this case. The basic idea behind this theory is that a particular input mode is represented by an equivalent transmission line model. In this description, all of the infinite number of waveguide modes have an equivalent transmission line model, with equivalent voltages and currents; though for non-TEM modes these quantities are not unique, as long as they are defined consistently it is a valid model. The input mode travels

down its transmission line and reaches an impedance composed of the other modes of the waveguide and the input impedance to the open-ended aperture antenna (see Fig. 3-3). Higher order modes and radiated free-space modes are created to satisfy the interface boundary conditions.

The radiated free-space modes are not included explicitly as a transmission line in this system, but are included in the input antenna impedance parameter: $Z_A = R_A + iX_A$, where R_A is the antenna resistance and X_A is the antenna reactance. The resistive component consists of two parts: R_r, the radiation resistance of the antenna representing the actual radiated power, and R_L, the loss resistance of the antenna representing ohmic losses. The reflection is then given by the impedance mismatch

$$r = \frac{Z_L - Z_1}{Z_L + Z_1}, \tag{3.16}$$

where Z_L is the load impedance as seen from transmission line 1. In practice, it is very difficult to calculate the antenna impedance because it requires accurate knowledge of the near field reactive fields [37]. This thesis resorts to a full-wave numerical analysis presented in Chapter 5 for the metal-metal waveguide and clearly shows the hybrid optical/microwave nature of the THz reflection problem.

3.4 Radiation Pattern and Directivity

The radiation pattern and directivity of edge-emitting lasers are necessary parameters to have in the application of the laser. For example, it is important to have knowledge of either the near-field or the far-field pattern (depending on the specific setup) in calculating the efficiency of coupling the laser's power into a fiber. Radiation patterns for traditional edge-emitting lasers, from the optical regime to the mid-infrared regime, are usually based on classical scalar theories of diffraction, which assume that the aperture size is much greater than the wavelength such that coupling effects at the boundary of the aperture may be ignored. Such techniques assume knowledge of the free-space fields in the immediate vicinity of the aperture and use techniques from

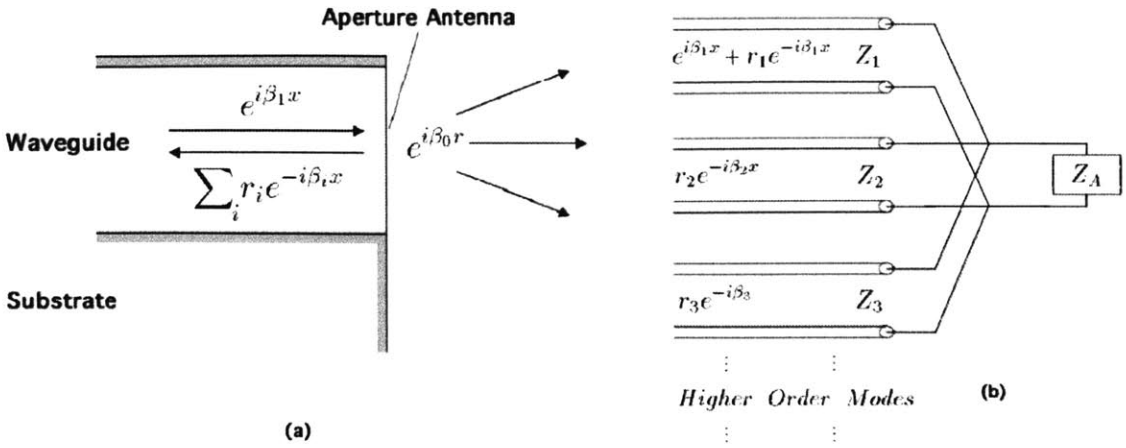

Figure 3-3: (a) Geometry representation of the metal-metal waveguide facet. (b) Transmission line model of the metal-metal waveguide facet; an input mode is sent down line 1, which, due to the impedance mismatch at the end, excites higher-order modes that travel back down the other transmission lines (though each mode has its own transmission line, they all represent they same physical waveguide in (a)).

Fourier optics in determining these patterns. However, for sub-wavelength apertures, the boundary effects of the aperture affect the radiated field patterns to the point of rendering scalar diffraction theories as not even capable of producing qualitative agreements [38]. Recent research in near-field microscopy [39, 40] and even up to the microwave regime [41] suggest that surface plasmons have a considerable effect on the transmission properties of sub-wavelength apertures. Numerical results of the radiation patterns for both the SI surface-plasmon waveguide and the metal-metal waveguide will be presented in Chapter 5.

Chapter 4

Waveguide Design and Analysis

4.1 Introduction

In this chapter, the SI surface-plasmon and metal-metal waveguides are introduced with their relevant variable parameters defined; both waveguides utilize the surface-plasmon as the confinement mechanism, which is discussed in more detail in Appendix B. Numerical results of THz QCL waveguide simulations are presented for each of these waveguiding structures. Critical values are identified for variable parameters, such as waveguide width, of both structures at which point deviations from one-dimensional analysis become non-negligible. Optimum values for other variable parameters, such as doping, are also identified which yield the best figure-of-merit, g_{th}. All two-dimensional simulations presented were carried out by the finite element method using FEMLAB. All one-dimensional simulations presented were carried out in MATLAB using a matrix formalism approach previously presented in Ref. [18].

4.2 Simulation Method

Waveguide simulations are fundamentally an eigenvalue problem and are solved in FEMLAB's two-dimensional perpendicular hybrid-mode solver (see Appendix A). Transverse electric (TE)- and transverse magnetic (TM)-mode solvers also exist in FEMLAB; however, due to the inherent nature of the inhomogeneity of the waveg-

uides in interest, the solutions will be a hybrid between TE and TM modes, and the former mode solver must be used. The term "perpendicular" refers to the fact that the eigenmode propagates perpendicular to the two-dimensional structure defined. The Drude model, discussed in Section 3.3.1, is used to calculate the complex permittivities that are entered into FEMLAB to define the material properties of the relevant geometries. In the solution of the waveguide problem, FEMLAB returns the eigenvalue $-\beta^2$, where β is the propagation constant of the eigenmode. From this, the waveguide loss is obtained by

$$\alpha_w = -2\mathrm{Im}\{\beta\}. \tag{4.1}$$

In these simulations, gain is not included in the permittivity of the active region. This is acceptable to the same degree that Eq. 3.3 defines the relationship between the modal gain and the active region gain. To be more accurate, a gain should be included in the active region of the structure such that an eigenvalue with no imaginary part is obtained; thus, $\alpha_w = 0$ and the eigenmode would propagate without loss. The true waveguide loss would then be $\alpha_w = -\Gamma g$, where g is the gain used in the active region. An iterative approach would need to be used in this case: the gain value would be adjusted at each iteration such that the loss eventually converges to zero. Such an approach is time consuming and only corrects the previous results to a small enough degree to be deemed negligible for our purposes. The confinement factor, Γ, is calculated by integrating the time-averaged Poynting vector over the respective domains as defined by Eq. 3.4.

The symmetry of these waveguides yields even and odd eigenmodes, with the fundamental eigenmode of interest being even. This inherent aspect of symmetric waveguides was taken advantage of by applying appropriate boundary conditions to the line of symmetry and simulating only one-half of the structure. Mesh structures were then able to be made more refined with the memory saved. For the even fundamental eigenmode, a perfect magnetic conductor boundary condition, discussed in Appendix A, was used at the line of symmetry.

Table 4.1: List of the SI surface-plasmon waveguide variables and their respective ranges for simulations carried out.

SI Surface-Plasmon Waveguide Variables

Pre-MBE Growth Variables	
Plasma Thickness	300 – 1000 nm
Plasma Doping	1.0 – 5.0×10^{18} cm^{-3}
Post-MBE Growth Variables	
Waveguide Width	30 – 250 μm
Substrate Thickness	10 – 200 μm
Side Contact Gap Distance	5 – 75 μm
Geometry	Dry vs. Wet

4.3 SI Surface-Plasmon Waveguide Design

As mentioned in Section 1.2, the SI surface-plasmon waveguide was the key development in the demonstration of the first terahertz QCLs [1, 2, 3]. The geometry of the SI surface-plasmon waveguide is shown in Fig. 4-1. The waveguide is based on a double-sided surface-plasmon between the upper metallic contact and the lower heavily doped plasma layer. Electrical contact is made possible by side metal contacts on top of the heavily doped plasma layer. The substrate is semi-insulating to prevent any extra loss due to modal overlap.

Due to the numerous variable parameters in the SI surface-plasmon, it is a non-trivial matter in optimizing and characterizing the dependencies that each has on the final figure-of-merit. The variables may be divided into pre- and post-MBE growth variables as listed in Table 4.1. Pre-MBE growth variables are set before the MBE growth of the structures; post-MBE growth variables are set after this step. Note that the range of the substrate thickness has been extended beyond reasonable post-MBE growth abilities only to analyze the results in a larger context. Other possible variables include the active region thickness and the active region doping. To keep the number of simulations to a reasonable number, these variables are set at 10 μm and 2×10^{15} cm^{-3}, respectively, for all simulations. The value of 2×10^{15} cm^{-3} is among the lowest carrier concentration of THz QCLs.

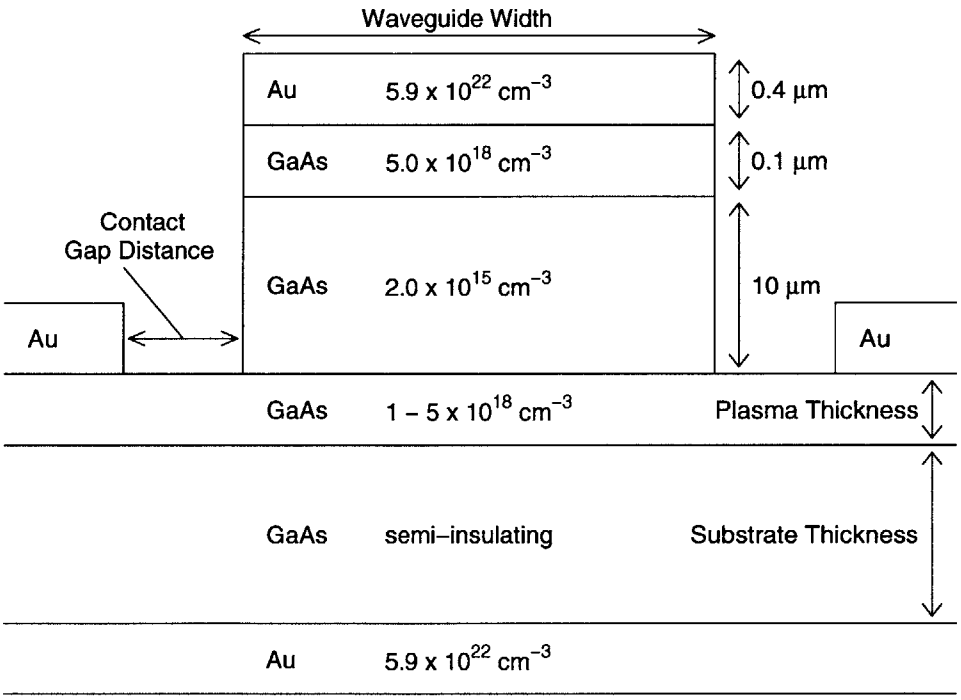

Figure 4-1: Schematic of the SI surface-plasmon waveguide's geometry. The structure consists of a top metal contact, a thin heavily doped GaAs injector layer, the active region, the GaAs plasma layer, the semi-insulating substrate, a bottom metal layer, and two side metal contacts.

4.4 SI Surface-Plasmon Waveguide Results

Simulations were carried out for the SI surface-plasmon waveguide over the variables defined in Table 4.1 for the following set of frequencies: 2.5, 3.0, 3.5, 4.0, 5.0, 6.0, and 7.0 THz. The waveguide's figure-of-merit is most sensitive to the pre-MBE growth variables and are considered first for each frequency. Once an optimum plasma doping level is determined, the waveguide width is then considered using this respective plasma doping level. Substrate thickness and side metal contact gap distance are considered next. All simulations, unless specifically noted, use a substrate thickness of 200 μm. In addition, aside from the side metal contact gap distance simulations themselves, all simulations neglect these side contacts by assuming their distances to the waveguide are large enough such that any perturbative effects produced by them are negligible. This made possible more memory allocation for mesh refinements in other parts of the geometry.

For each set of simulations, the values for α_w, Γ, and $(\alpha_w + \alpha_m)/\Gamma$ are tabulated, where the latter is the threshold gain, g_{th}, the waveguide's final figure-of-merit. The mirror loss, α_m, for all SI surface-plasmon waveguide simulations assumes a cavity length of 3 mm and a mirror reflectivity of 0.3195 (from the effective index method and $n_{\text{eff}} = 3.6$). This mirror reflectivity is an acceptable value to use as described in Section 5.3. A 3 mm length bar is equivalent to a 1.5 mm length bar with one facet coated with a high-reflection (HR) material.

4.4.1 Plasma parameters

Figs. 4-2(a)-4-8(a), for frequencies ranging from 2.5–7 THz, overlay previous one-dimensional calculations of α_w, Γ, and $(\alpha_w + \alpha_m)/\Gamma$ with two-dimensional calculations of selected waveguide widths for comparison. The plasma layer thickness closely correlates to the confinement factor and overall loss. While a thicker plasma layer yields a higher confinement factor up to a value of $\Gamma \sim 0.5$, it also increases the modal overlap with itself and, in turn, increases the loss. A compromise must be made between the two to find the optimum value. For frequencies above 3.0 THz,

no compromise is needed as the thinnest plasma layer simulated, 300 nm, gives the optimum values in the one-dimensional calculations. However, the effects of finite waveguide widths, as discussed in the next section, predict that thicker plasma layers yield a better figure-of-merit below certain waveguide widths. While the waveguide loss decreases as the frequency decreases, due to the laser frequency moving further away from the bulk plasma frequency of the plasma layer, the confinement factor also decreases, because the active region thickness to wavelength ratio decreases. These would tend to balance each other out in calculating the gain threshold condition except for the inclusion of the mirror coupling loss, which is assumed not to change with frequency for the SI surface-plasmon waveguide. Therefore, while α_w decreases with the frequency, α_m does not and for frequencies below 3.0 THz, thin plasma layers yield higher gain threshold conditions than do thicker plasma layers. The optimum plasma doping level is seen to decrease from the maximum value of 5.0×10^{18} cm^{-3} at 7 THz to 1.0×10^{18} cm^{-3} at 2.5 THz.

Two generalized statements can be made in comparing one-dimensional and two-dimensional plasma layer parameter effects on the final figure-of-merit. First, the optimum doping level is seen to decrease with a narrower waveguide width from a maximum optimum value given by one-dimensional analysis. For example, at a frequency of 5 THz and a plasma layer thickness of 0.3 μm (see Fig. 4-4(a)), the optimum doping level goes from 4.0×10^{18} cm^{-3} in the one-dimensional (infinite waveguide width) case to 1.5×10^{18} cm^{-3} for a finite waveguide width of 60 μm. Second, in cases where thin plasma layers are used for narrow waveguides, the optimal plasma layer thickness is greater than that given by one-dimensional analysis in order to compensate for the lower confinement factor. This is discussed in the next section on waveguide width effects.

4.4.2 Waveguide width

Figs. 4-2(b)-4-8(b), for frequencies ranging from 2.5–7 THz, show the effects of waveguide width using the optimal plasma doping levels determined from Figs. 4-2(a)-4-8(a). For all frequencies, three cases of plasma thicknesses are displayed for compar-

ison; critical waveguide widths can be inferred from these simulations in which the finite width of the waveguide begins to have deviating effects from one-dimensional calculations.

For purposes of designing narrow waveguides, it is clear that choosing a thin plasma layer degrades the final figure-of-merit. Thicker plasma layers are able to preserve the confinement of the mode more efficiently for small waveguide widths and this compensates for their greater loss contributions. This statement becomes more applicable with decreasing frequency as seen clearly for the case that f = 3.0 THz, shown in Fig. 4-7(b). One-dimensional analysis shows that a plasma layer 0.4 μm thick gives a lower gain threshold condition than a plasma layer 0.8 μm thick; however, a 0.4 μm plasma layer thickness is seen not capable of supporting a mode with a waveguide width of 160 μm, while a 0.8 μm plasma layer thickness can still support a mode down to a waveguide thickness of 75 μm.

For the sets of simulations at 3.5, 4.0, and 5.0 THz (Figs. 4-4(b)-4-6(b)), two sets of simulations with different doping levels are overlaid for the final figure-of-merit to illustrate that the optimum doping level decreases with decreasing waveguide width. For example, at 4 THz, the optimum doping level given by one-dimensional analysis is $\sim 2.5 \times 10^{18}$ cm^{-3}. From Fig. 4-5(b), for a waveguide width of 50 μm and a plasma layer thickness of 0.7 μm, the figure-of-merit is approximately 30% less by using a smaller doping level of 1.5×10^{18} cm^{-3}.

While these simulations were carried out for dry-etched waveguides, in which the side walls are vertical, they have also been shown in simulations to be valid for wet-etched geometries, in which the side walls are angled depending on the specific processing recipe. For wet-etched waveguides, an effective waveguide width has to be determined and is close to the average of the top and bottom widths of the waveguide.

4.4.3 Substrate thickness

Aside from the waveguide perspective, thin substrates offer thermal advantages for device operation. However, it is shown that in some cases of narrow waveguide widths, thinning the substrate will increase the gain threshold condition. Figs. 4-

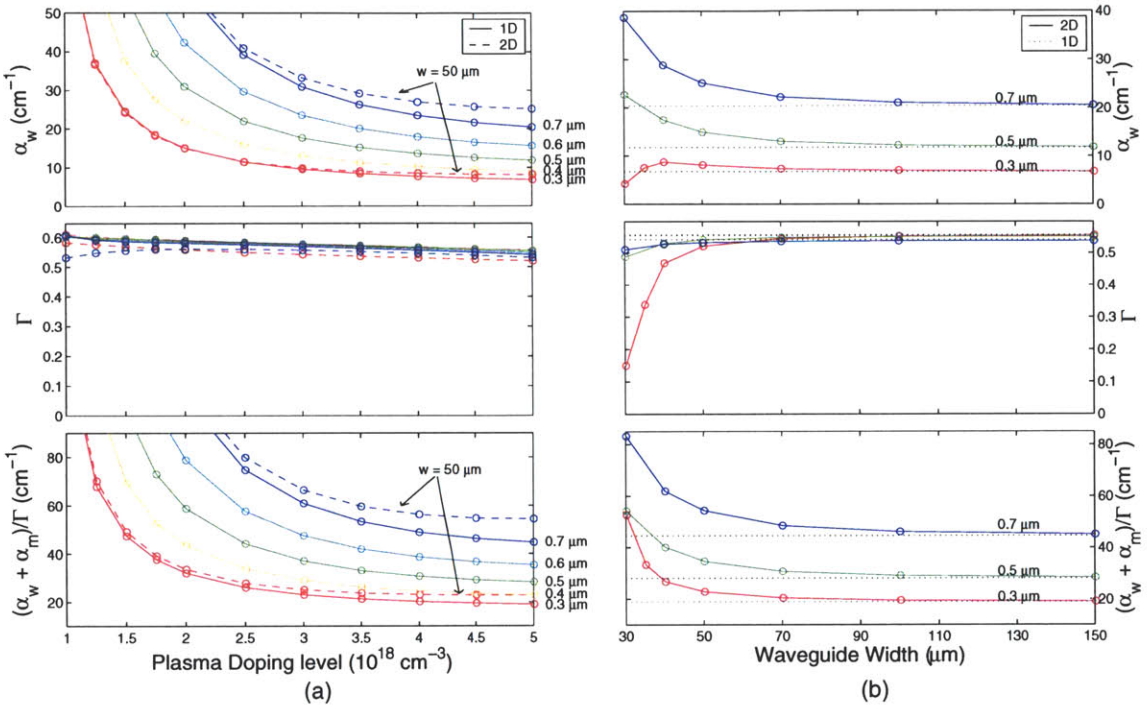

Figure 4-2: SI surface-plasmon waveguide simulation results at f = 7.0 THz: (a) 1D loss and confinement factors vs. plasma doping for plasma thicknesses of 0.3–0.7 μm; overlaid are 2D results for a waveguide width of 50 μm at plasma thicknesses of 0.3 and 0.7 μm. (b) 2D loss and confinement factors vs. waveguide width for plasma thicknesses of 0.3–0.7 μm and a plasma doping of 5×10^{18} cm^{-3}; 1D results are plotted to show convergence.

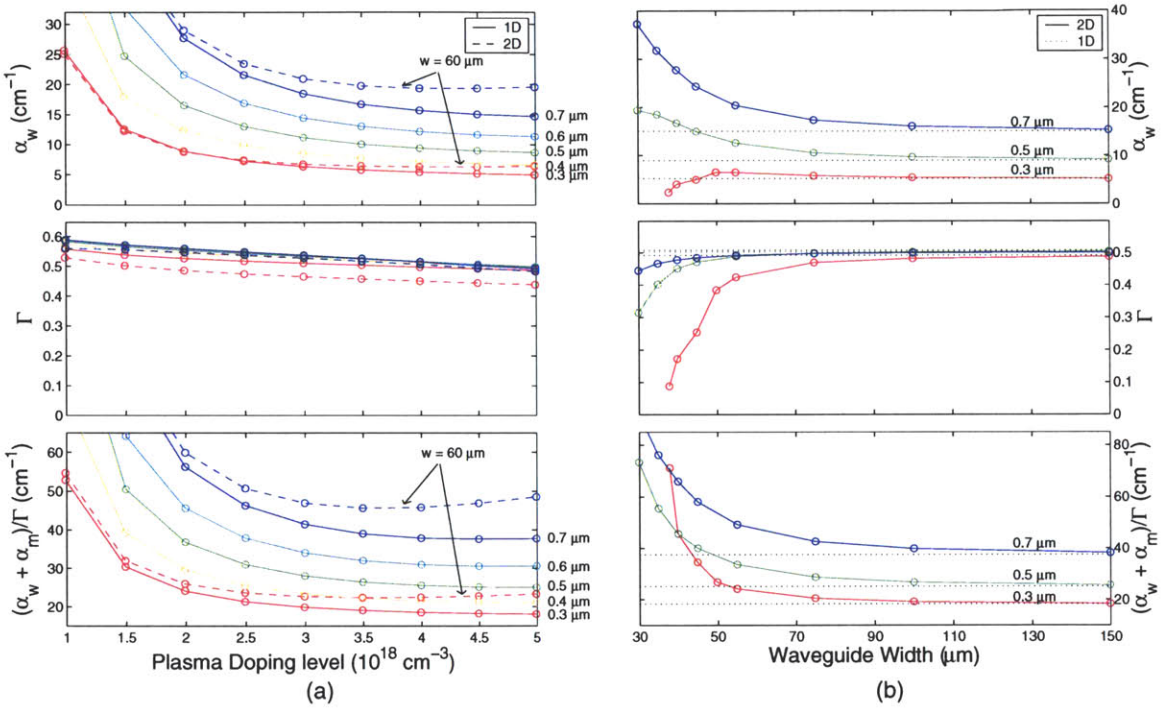

Figure 4-3: SI surface-plasmon waveguide simulation results at f = 6.0 THz: (a) 1D loss and confinement factors vs. plasma doping for plasma thicknesses of 0.3–0.7 μm; overlaid are 2D results for a waveguide width of 60 μm at plasma thicknesses of 0.3 and 0.7 μm. (b) 2D loss and confinement factors vs. waveguide width for plasma thicknesses of 0.3–0.7 μm and a plasma doping of 4.5×10^{18} cm^{-3}; 1D results are plotted to show convergence.

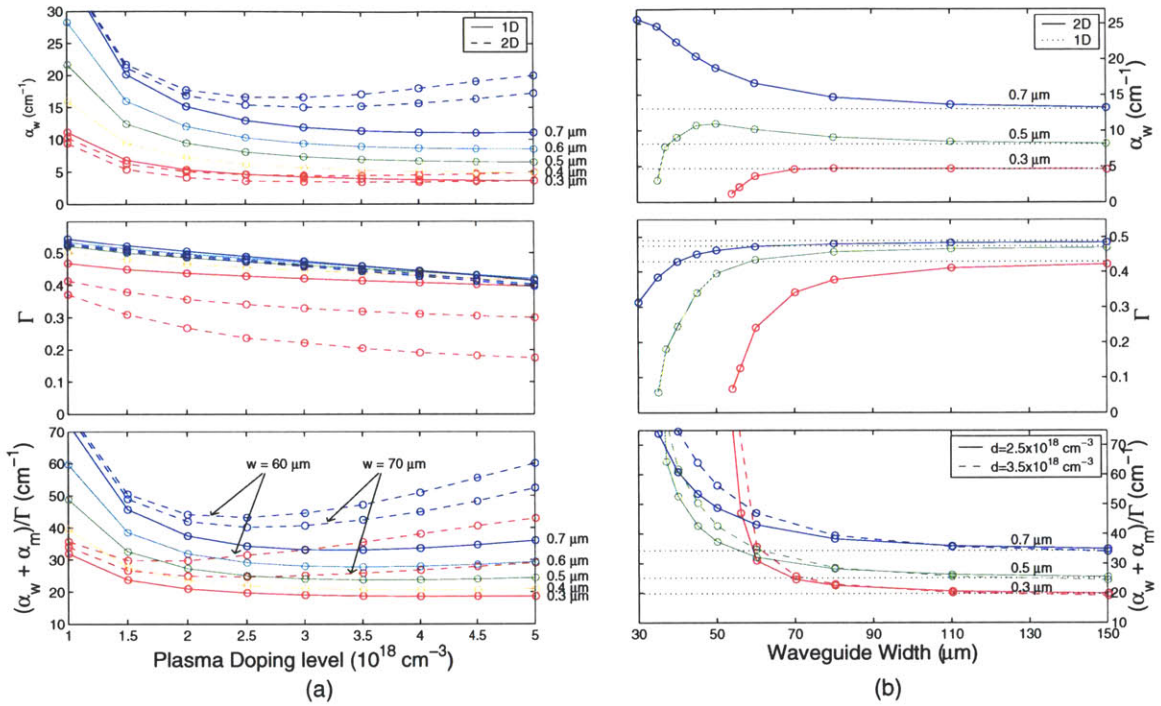

Figure 4-4: SI surface-plasmon waveguide simulation results at f = 5.0 THz: (a) 1D loss and confinement factors vs. plasma doping for plasma thicknesses of 0.3–0.7 μm; overlaid are 2D results for waveguide widths of 60 and 70 μm at plasma thicknesses of 0.3 and 0.7 μm. (b) 2D loss and confinement factors vs. waveguide width for plasma thicknesses of 0.3–0.7 μm and a plasma dopings of 2.5 and 3.5×10^{18} cm^{-3}; 1D results are plotted to show convergence. Solid lines in all three figures in (b) correspond to a plasma doping level of 2.5×10^{18} cm^{-3}.

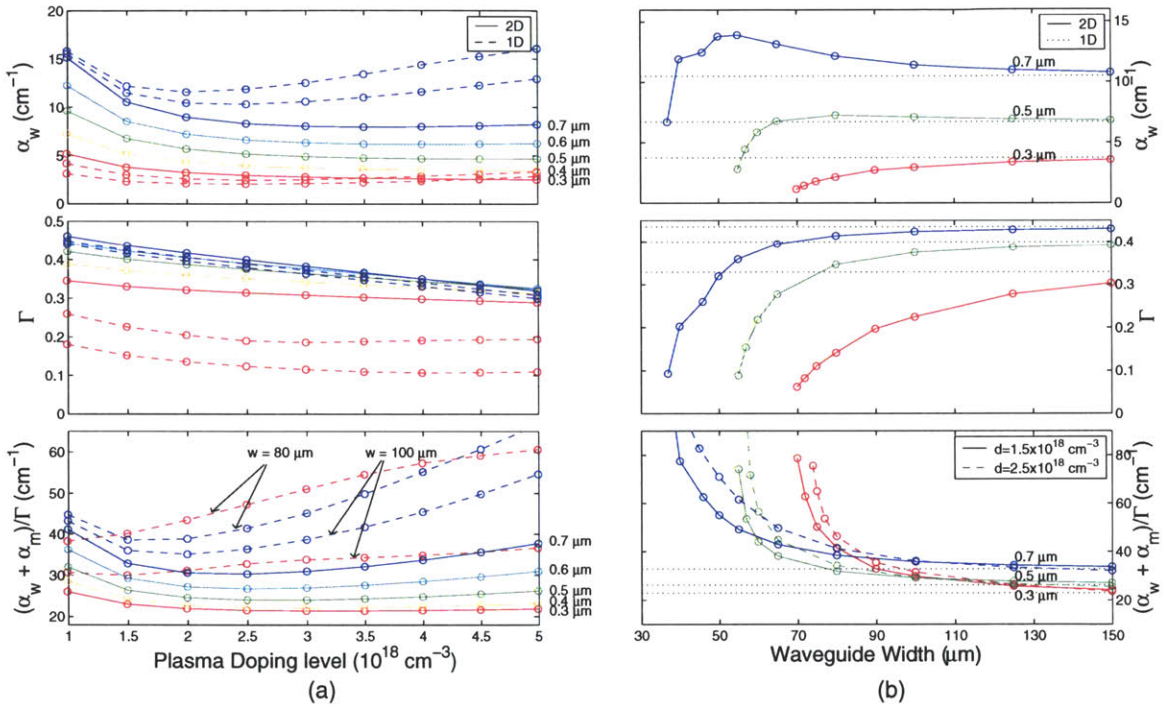

Figure 4-5: SI surface-plasmon waveguide simulation results at f = 4.0 THz: (a) 1D loss and confinement factors vs. plasma doping for plasma thicknesses of 0.3–0.7 μm; overlaid are 2D results for waveguide widths of 80 and 100 μm at plasma thicknesses of 0.3 and 0.7 μm. (b) 2D loss and confinement factors vs. waveguide width for plasma thicknesses of 0.3–0.7 μm and a plasma dopings of 1.5 and 2.5 $\times$ 10^{18} cm^{-3}; 1D results are plotted to show convergence. Solid lines in all three figures in (b) correspond to a plasma doping level of 1.5 $\times$ 10^{18} cm^{-3}

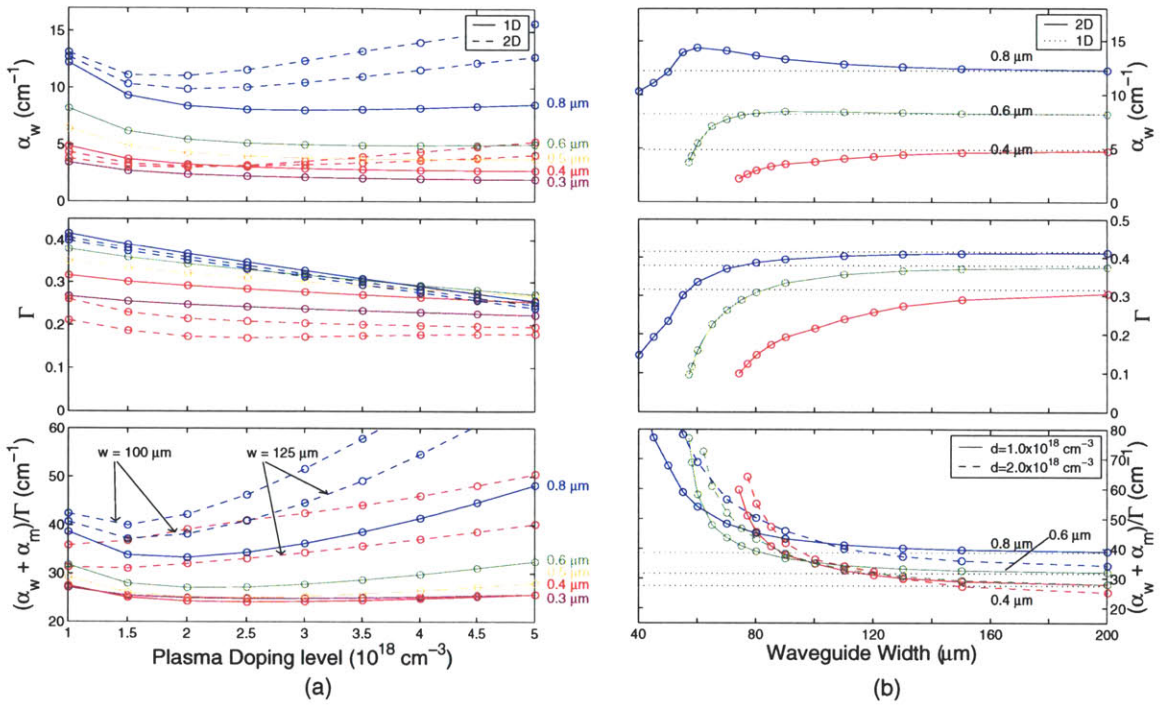

Figure 4-6: SI surface-plasmon waveguide simulation results at f = 3.5 THz: (a) 1D loss and confinement factors vs. plasma doping for plasma thicknesses of 0.3–0.8 μm; overlaid are 2D results for waveguide widths of 100 and 125 μm at plasma thicknesses of 0.4 and 0.8 μm. (b) 2D loss and confinement factors vs. waveguide width for plasma thicknesses of 0.4–0.8 μm and a plasma dopings of 1.0 and 2.0 $\times$ 10^{18} cm^{-3}; 1D results are plotted to show convergence. Solid lines in all three figures in (b) correspond to a plasma doping level of 1.0 $\times$ 10^{18} cm^{-3}

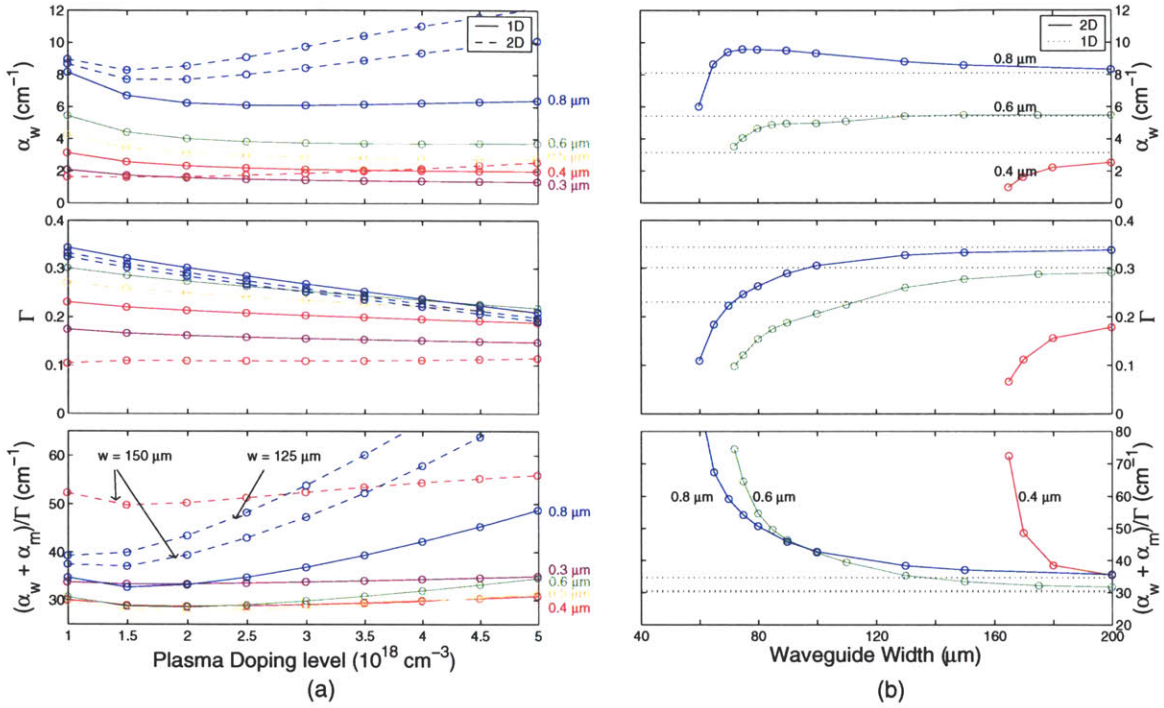

Figure 4-7: SI surface-plasmon waveguide simulation results at f = 3.0 THz: (a) 1D loss and confinement factors vs. plasma doping for plasma thicknesses of 0.4–0.8 μm; overlaid are 2D results for waveguide widths of 125 and 150 μm at plasma thicknesses of 0.4 and 0.8 μm. (b) 2D loss and confinement factors vs. waveguide width for plasma thicknesses of 0.4–0.8 μm and a plasma doping of 1.0×10^{18} cm^{-3}; 1D results are plotted to show convergence.

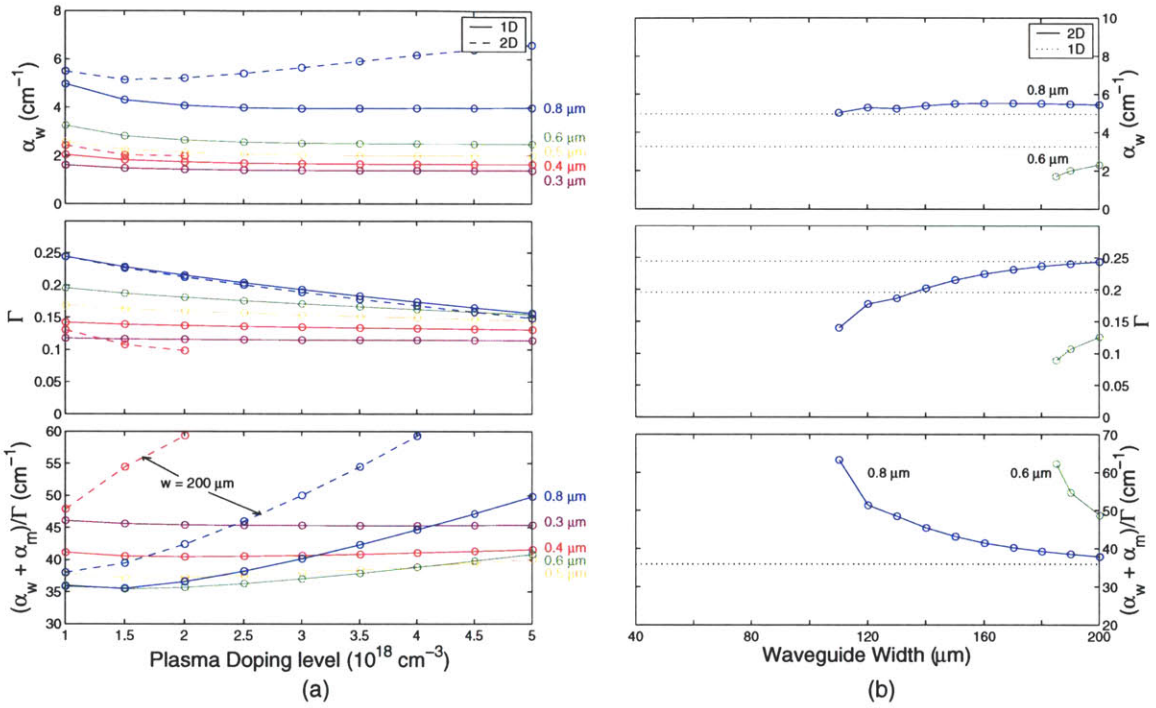

Figure 4-8: SI surface-plasmon waveguide simulation results at f = 2.5 THz: (a) 1D loss and confinement factors vs. plasma doping for plasma thicknesses of 0.4–0.8 μm; overlaid are 2D results for a waveguide width of 200 μm at plasma thicknesses of 0.4 and 0.8 μm. (b) 2D loss and confinement factors vs. waveguide width for plasma thicknesses of 0.6–0.8 μm and a plasma doping of 1.0×10^{18} cm^{-3}; 1D results are plotted to show convergence.

9 and 4-10 show the effect of varying the substrate thickness for varying frequencies and waveguide widths. As the waveguide width decreases, the confinement of the mode degrades and allows stronger coupling to the surface-plasmon on the bottom metal contact. With thin substrates, this coupling with the bottom contact's surface plasmon is increased (see Fig. 4-11). At some point for thin enough plasma layers or narrow enough waveguide widths, there exists a range of substrate thickness in which the gain threshold blows up and no eigenmode is found. This is counter to the original notion that thin substrates will act more like a metal-metal waveguide and therefore provide higher confinement. It is only below certain substrate thicknesses in which this analogy with the metal-metal waveguide begins to converge. For these intermediate substrate thicknesses in which the mode is slightly leaky (meaning the mode is close to be being a substrate radiation mode [42]), the interaction of the mode with the bottom surface-plasmon is sufficiently strong to lower the confinement factor enough such that the overall figure-of-merit blows up. However, for cases of low frequencies, as seen for the 2.5 THz case in Fig. 4-10(c), the mode is slightly leaky and if it is possible with available processing capabilities, it can be advantageous to thin the waveguide in order to minimize the leak.

4.4.4 Side metal contact gap distance

Fig. 4-12 shows the effects of the side metal contact-to-waveguide gap distance for three frequencies. Gap distances below certain values show coupling effects (seen in Fig. 4-13) with the surface-plasmons associated with the metal contacts. The widths of the side metal contacts were set at 200 μm for these simulations. It is clear that for gap distances below 20 μm the coupling effects greatly degrade the figure of merit. This quantitatively verifies the justification for the increase in gap distance made by Ajili in Ref. [19] to decrease modal overlap with the metal contacts.

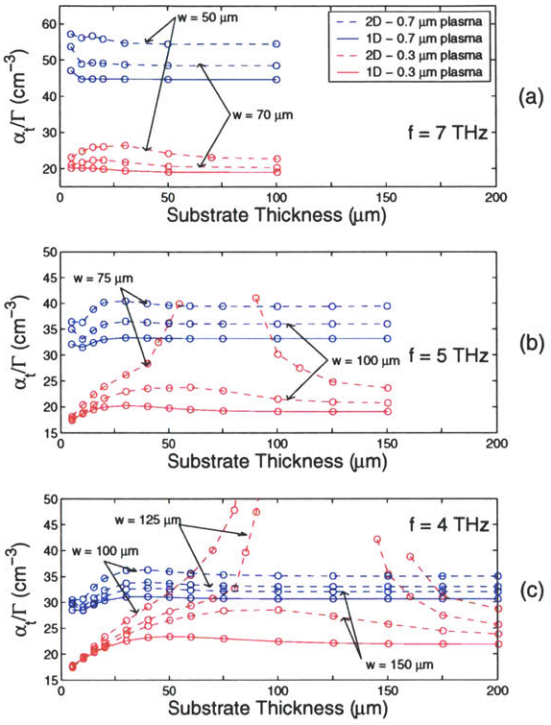

Figure 4-9: SI surface-plasmon waveguide simulation results of 1D and 2D loss and confinement factors vs. substrate thickness. Waveguides with finite widths of various values are labeled. Plasma thicknesses of 0.3 and 0.7 μm were used; plasma doping levels were set at (a) 5×10^{18} cm^{-3} for f = 7 THz, (b) 3×10^{18} cm^{-3} for f = 5 THz, and (c) 2×10^{18} cm^{-3} for f = 4 THz.

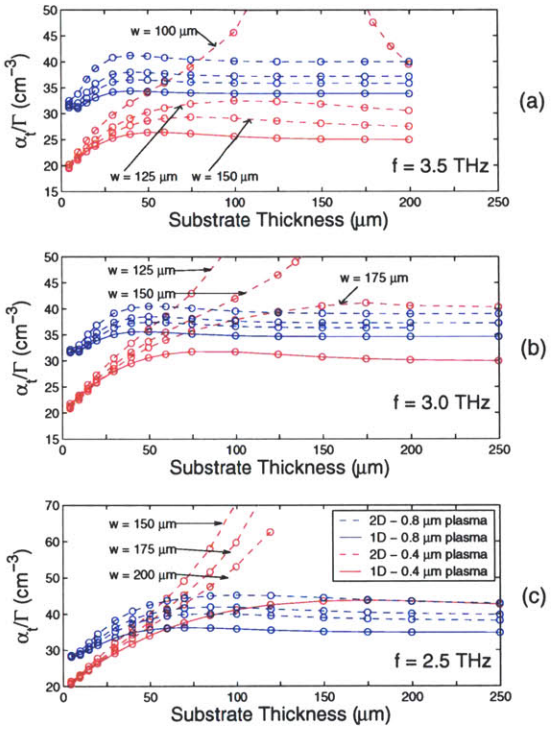

Figure 4-10: SI surface-plasmon waveguide simulation results of 1D and 2D loss and confinement factors vs. substrate thickness. Waveguides with finite widths of various values are labeled. Plasma thicknesses of 0.4 and 0.8 μm were used; plasma doping levels were set at (a) 1.5×10^{18} cm^{-3} for f = 3.5 THz, (b) 1×10^{18} cm^{-3} for f = 3 THz, and (c) 1×10^{18} cm^{-3} for f = 2.5 THz.

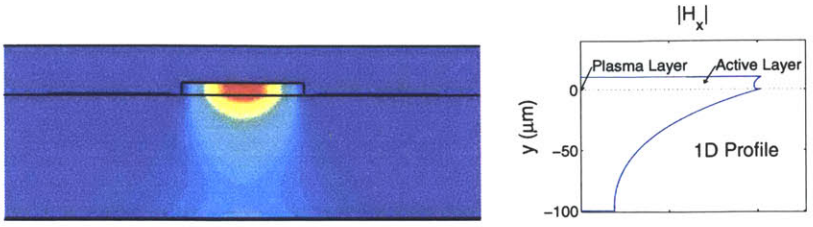

(a) substrate thickness = 100 μm

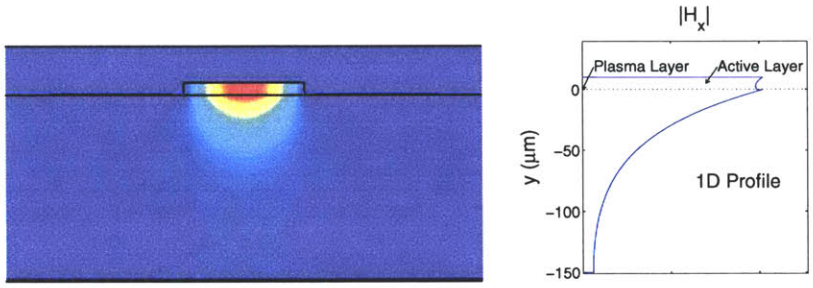

(b) substrate thickness = 150 μm

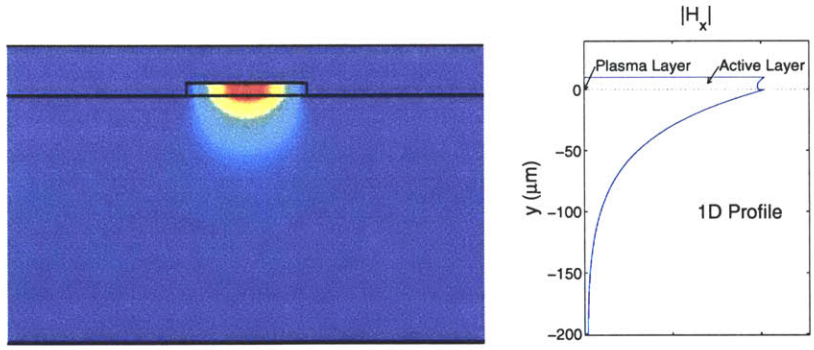

(c) substrate thickness = 200 μm

Figure 4-11: (a)-(c) represent a series of two-dimensional field profiles of the fundamental eigenmode along with their one-dimensional profile as the thickness of the substrate is varied. The frequency is 4 THz, the waveguide width is 150 μm, and the plasma layer is 0.3 μm thick and doped at 2.0×10^{18} cm^{-3}.

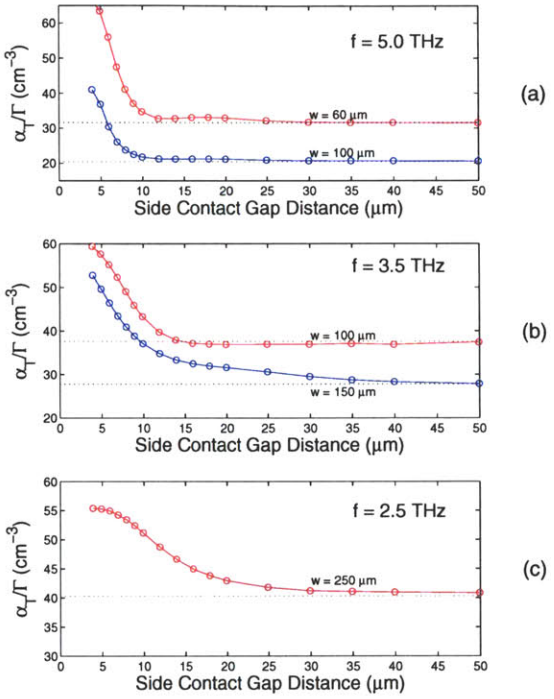

Figure 4-12: SI surface-plasmon waveguide simulation results for 1D and 2D loss and confinement factors vs. side contact gap distance: (a) f = 5.0 THz with a plasma thickness of 0.3 μm doped at 3×10^{18} cm^{-3}, (b) f = 3.5 THz with a plasma thickness of 0.4 μm doped at 1.5×10^{18} cm^{-3}, (c) f = 2.5 THz with a plasma thickness of 0.6 μm doped at 1×10^{18} cm^{-3}. Waveguide widths are noted in each case.

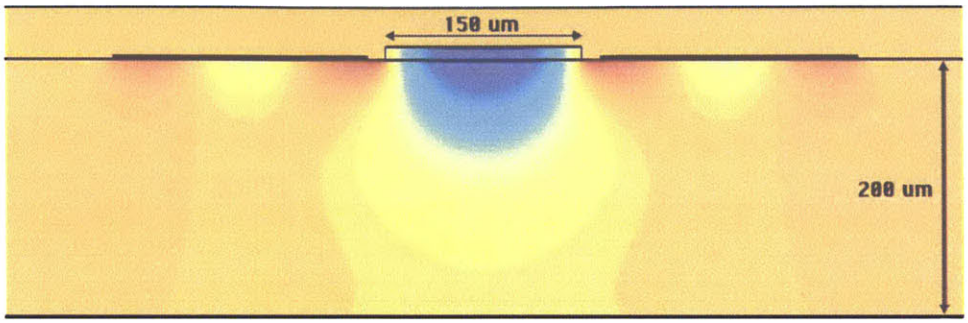

(a) gap distance = 15 μm

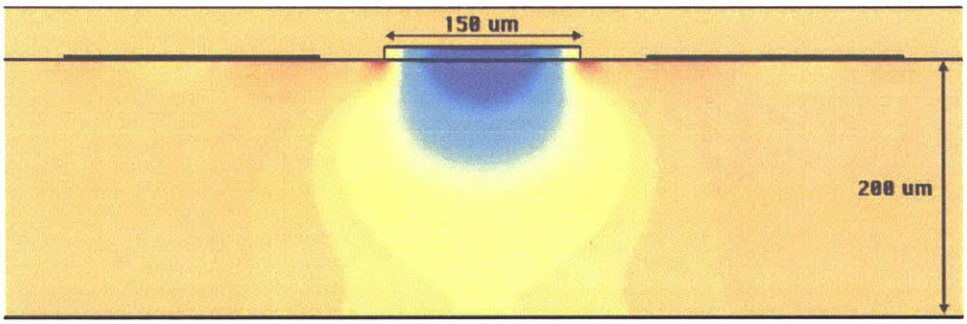

(b) gap distance = 50 μm

Figure 4-13: (a)-(b) show two field profiles of the fundamental eigenmode with two different side metal contact to waveguide distances. The frequency is 3.5 THz, the waveguide width is 150 μm, the substrate thickness is 200 μm, and the plasma layer is 0.5 μm thick doped at 1.5×10^{18} cm^{-3}.

Table 4.2: List of the metal-metal waveguide variables and their respective ranges for simulations carried out.

Metal-metal Waveguide Variables

Active Region Thickness	3 – 10 μm
Waveguide Width	30 – 150 μm

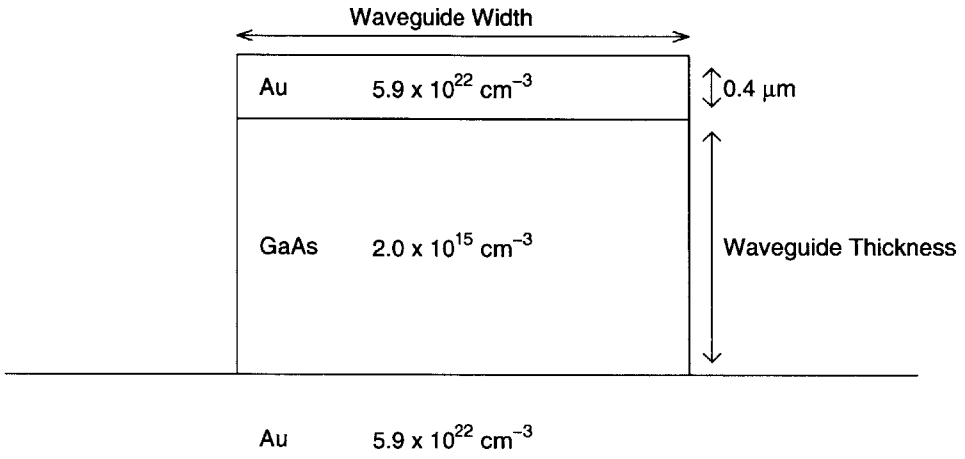

Figure 4-14: Schematic of the metal-metal waveguide's geometry. The structure consists of a top metal contact, the active region, and a bottom metal substrate.

4.5 Metal-Metal Waveguide Design

The geometry of the metal-metal waveguide is shown in Fig. 4-14. The waveguide, like the SI surface-plasmon waveguide, is based on a double-sided surface-plasmon between the top and bottom metallic contacts. The metal-metal waveguide has considerably less variables to consider than does the SI surface-plasmon waveguide and are listed in Table 4.2. The active region doping is another possible variable; however, it is set at 2×10^{15} cm^{-3}.

4.6 Metal-Metal Waveguide Results

Simulations were carried out for the metal-metal waveguide over the variables defined in Table 4.2 for the following set of frequencies: 1.0, 1.5, 2.0, 2.5, 3.0, 4.0, 5.0, and 7.0 THz. Unlike the SI surface-plasmon waveguide, the metal-metal waveguide has no pre-MBE growth variables to optimize, and considerably fewer processing variables to analyze. Effects of the waveguide width and active region thicknesses on the final figure-of-merit are presented.

Figs. 4-15 and 4-16 show the results of these simulations. For each set of simulations, the values for α_w, Γ, and $(\alpha_w + \alpha_m)/\Gamma$ are tabulated, where the latter is the gain threshold condition. The mirror loss, α_m, for each set of simulations depends on the frequency and the thickness of the active region as described in Section 5.4 and uses two-dimensional values calculated in that section (see Fig. 5-4). The cavity length is set to 3 mm. The mirror reflectivities for metal-metal waveguides are greater than those for SI surface-plasmon waveguides; therefore, the mirror coupling losses contribute less to the overall loss for metal-metal waveguides. In addition, since the confinement factors for all metal-metal waveguides are close to unity, the final figure-of-merit can be well approximated as simply the waveguide loss, α_w.

The waveguide loss is seen to increase as the active region thickness decreases; this increase in loss is due to an increase in modal coupling with the surface plasmons associated with the metal contacts. For low frequencies, as the lasing frequency approaches the bulk plasma frequency of the active region (0.43 THz), waveguide losses in the metal-metal waveguide become predominately due to free carrier loss associated with carriers in the active region itself. As seen by the decreasing sensitivity to the active region thickness, losses associated with the surface plasmons at the metal contacts become less important.

In comparison with the SI surface-plasmon, the metal-metal waveguide is seen to have little dependence on the width of the waveguide. In addition, the metal-metal waveguide not only is capable of maintaining low gain threshold conditions for waveguide widths much less than the lasing free-space wavelength, but also outperforms the

SI surface-plasmon waveguide for all waveguide widths, with little variation.

4.7 Discussions

Two-dimensional simulation results for SI surface-plasmon and metal-metal waveguides in the THz regime have been presented. Two-dimensional analysis has been compared to previous one-dimensional analysis and quantify when certain variable waveguide parameters begin to have non-negligible effects in two dimensions. For the SI surface-plasmon waveguide, the finite width of the waveguide has a considerable effect on the final figure-of-merit, and optimum plasma parameters are seen to differ from one-dimensional analysis. While some improvements may be possible in the design of SI surface-plasmon waveguides, such as gradually doping the plasma layer [43], it performs poorly in comparison with the metal-metal waveguide. The main obstacle in obtaining low gain threshold conditions for the SI surface-plasmon waveguide is its poor ability to confine the mode, yielding confinement values of $\Gamma = .1$–$.6$, especially at the lower frequencies. The metal-metal waveguide, on the other hand, is seen to exhibit little dependence on the waveguide width, has confinement factors close to unity, and yields lower loss factors across the frequency range investigated (1–7 THz). However, while the metal-metal waveguide outperforms the SI surface-plasmon waveguide in terms of waveguiding, it underperforms in terms of its ability to couple power out. This issue is discussed in the next chapter.

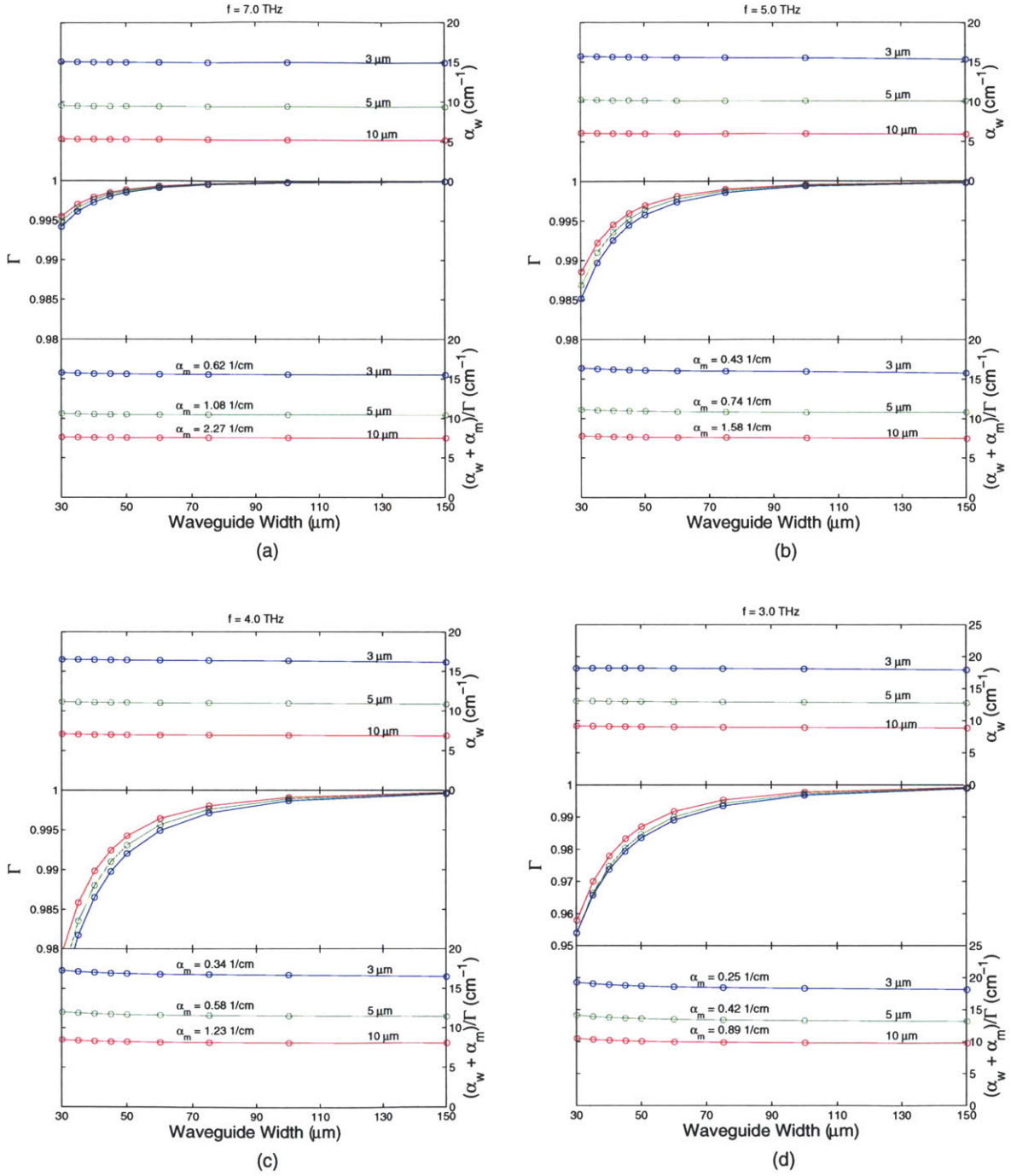

Figure 4-15: Metal-metal waveguide simulation results: 2D loss and confinement factors vs. waveguide width for core thicknesses of $3, 5$, and 10 μm for (a) f = 7.0 THz, (b) f = 5.0 THz, (c) f = 4.0 THz, and (d) f = 3.0 THz.

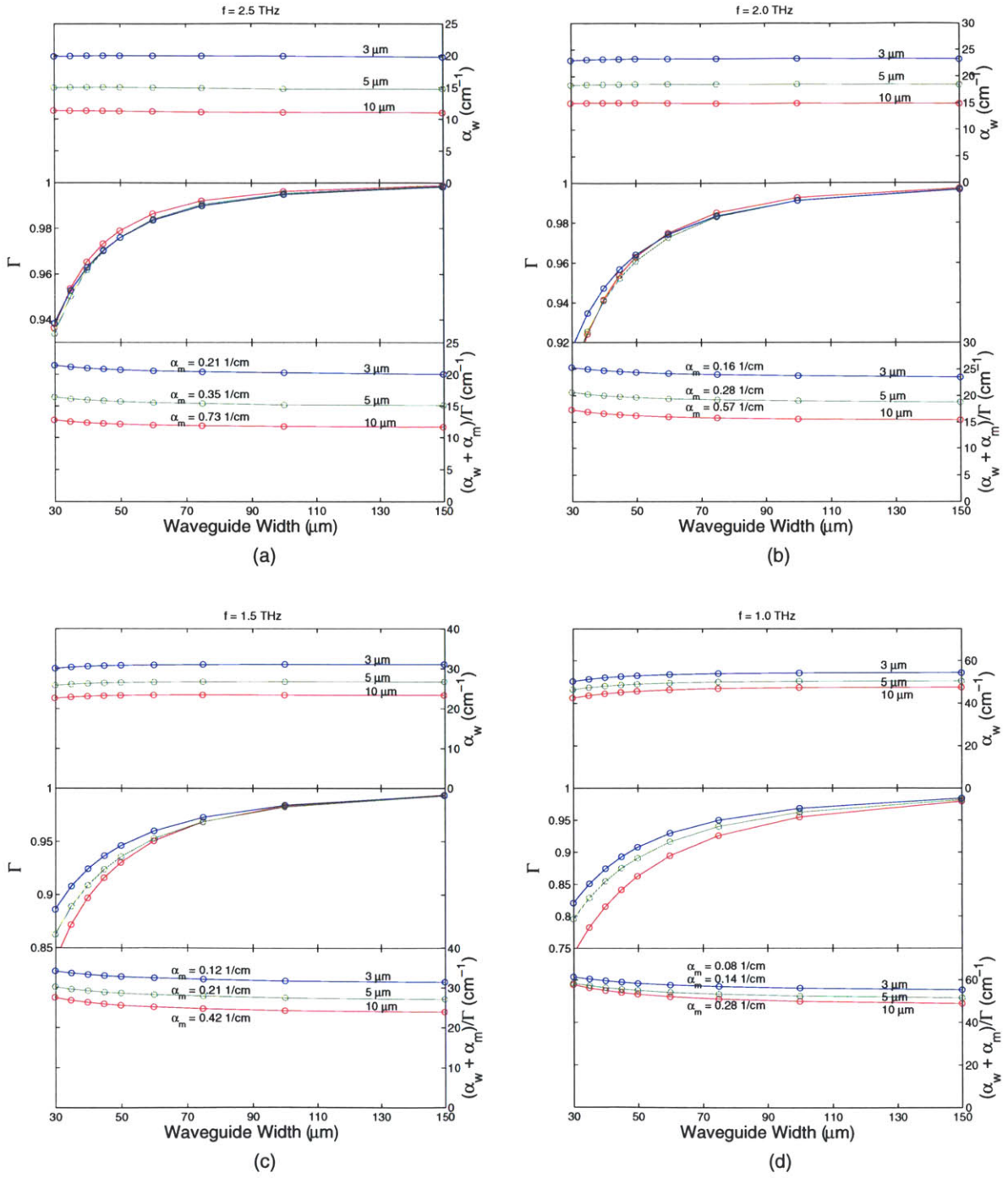

Figure 4-16: Metal-metal waveguide simulation results: 2D loss and confinement factors vs. waveguide width for core thicknesses of $3, 5$, and 10 μm for (a) f = 2.5 THz, (b) f = 2.0 THz, (c) f = 1.5 THz, and (d) f = 1.0 THz.

Chapter 5

Resonator Analysis

5.1 Introduction

The resonator of a laser includes both the waveguide and mirrors. The SI surface-plasmon and metal-metal waveguides were discussed in the previous chapter. This chapter focuses on the mirror reflectivity and the radiation pattern of the laser. The mirrors for both waveguides are simply constructed by cleaving the waveguides; the resulting facets, due to the orientation of the crystalline lattice, are approximately perfect planes.

5.2 Simulation Method

Two-dimensional facet simulations (where the width of the waveguide is inherently infinite) were performed in FEMLAB's in-plane TM wave mode solver. The term "in-plane" refers to the fact that the wave vectors are in the plane of the two-dimensional structure defined. Three-dimensional facet simulations were performed in FEMLAB's three-dimensional electromagnetic wave mode solver (see Appendix A). Matched boundary conditions (BCs) were used to excite a particular input eigenmode of the waveguide. Excitation of a mode is achieved by defining source terms on the boundary and associating their phases with a given propagation constant; this is described in more depth in Section A.2.1. The matched BC also acts as a perfectly absorbing

BC for any eigenmode traveling in the opposite direction due to reflection from the facet. For two-dimensional metal-metal resonator simulations, the input eigenmode is analytically derivable as simply the parallel-plate waveguide eigenmodes. For the three-dimensional metal-metal resonator simulations, the input eigenmode had to be simultaneously solved in the two-dimensional perpendicular hybrid mode solver for the corresponding structure and coupled into the three-dimensional solver as the input. For the two-dimensional SI surface-plasmon resonator simulations, the input eigenmode was solved for by using the one-dimensional slab-waveguide technique and coupling the solved one-dimensional mode into FEMLAB from MATLAB.

To simplify the metal-metal resonator simulations, all materials were made lossless and the metals were replaced with perfect electrical conductor BCs. This was unnecessary in two dimensions; however, for the three-dimensional metal-metal resonator simulations, the memory requirements disallowed any extra mesh allotment to cover the metal surfaces. For consistency, both two- and three-dimensional metal-metal resonator simulations were therefore made lossless.

Due to the inherent nature of the SI surface-plasmon mode, it would be impossible in the resonator simulations to make the materials lossless. Therefore, a gain had to be included in the active region such that the input eigenmode did not decay before reaching the facet. This gain value was determined from the one-dimensional calculations such that the waveguide loss was made to be zero. Unfortunately, due to the severe aspect ratio in the SI surface-plasmon waveguide structure and the severe memory limitations in full-wave three-dimensional numerical processing, no simulations were able to be performed in three dimensions for the SI surface-plasmon waveguide.

5.2.1 Reflectivity calculation

A simple method to determine the reflection of the facet is to divide the reflected power, P_{r}, by the input power, P_{input}. However, in two-dimensional simulations, for waveguides with more than one propagating mode the reflected power is usually carried by more than one mode of the waveguide due to higher-order excitations at

the facet; higher-order modes with an imaginary propagation constant are evanescent and do not carry power. However, in three dimensions, evanescent modes, due to the finite width of the waveguide, are leaky and do carry power away laterally. For our gain threshold condition, Eq. 3.5, the relevant parameter is the reflection coefficient into that particular mode and not including any reflections into higher order modes; therefore this method of calculating the power reflection is not always adequate.

The standing-wave ratio (SWR) method is an accurate way of determining the reflectivity of a specific input mode. In this method we assume a particular input mode, $\mathbf{h}_1(x,y)e^{i\beta_1 z}$, traveling in the z direction. Higher-order modes are excited at the facet to give a total field in the waveguide as

$$\mathbf{H}(x,y,z) = \mathbf{h}_1(x,y)e^{i\beta_1 z} + \sum_i r_i \mathbf{h}_i(x,y)e^{-i\beta_i z}, \tag{5.1}$$

where r_i is the reflection coefficient for each respective mode. By exploiting the inherent orthogonality of the eigenmodes, we can take the inner product of the full field with the input mode we are interested in and find its absolute value to be

$$|\langle \mathbf{h}_1(x,y)|\mathbf{H}(x,y,z)\rangle| = \left|\iint \mathbf{H}(x,y,z)\mathbf{h}_1^*(x,y)\, dxdy\right| = |1 + r_1 e^{-i2\beta_1 z}|, \tag{5.2}$$

where normalization is irrelevant as will be seen. The SWR is defined by the ratio of the maximum to minimum value of the standing-wave defined by Eq. 5.2

$$\mathrm{SWR} = \frac{|\langle \mathbf{h}_1|\mathbf{H}\rangle|_{\max}}{|\langle \mathbf{h}_1|\mathbf{H}\rangle|_{\min}} = \frac{1+|r_1|}{1-|r_1|}. \tag{5.3}$$

The calculation of the facet reflectivity therefore only needs the maximum and minimum values of the standing-wave defined in Eq. 5.2 to obtain a value of

$$R = |r_1|^2 = \left(\frac{\mathrm{SWR}-1}{\mathrm{SWR}+1}\right)^2. \tag{5.4}$$

A typical standing wave is shown in Fig. 5-1 over a length of one wavelength. By defining appropriate lines of integration in two dimensions and planes of integration

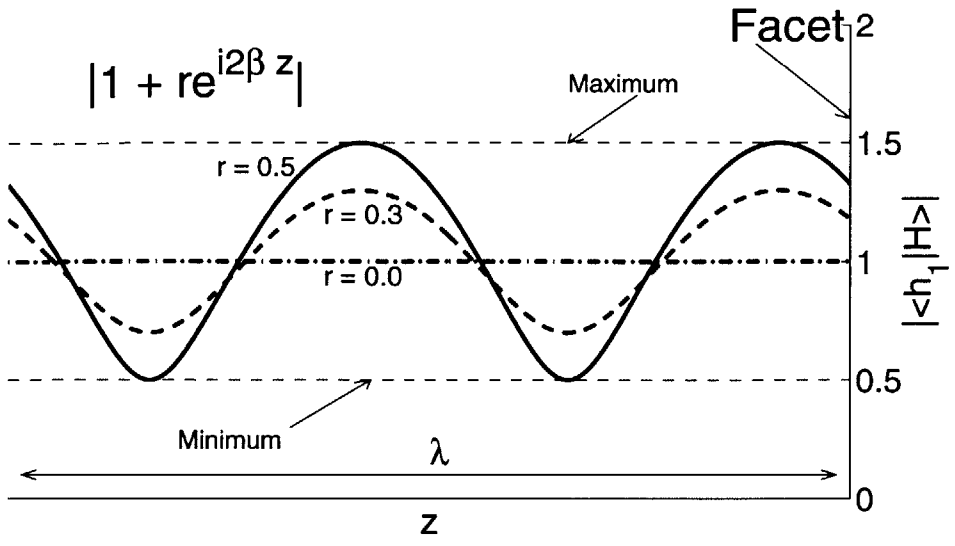

Figure 5-1: Typical standing-wave profiles over one wavelength for three values of the reflection coefficient: 0.0, 0.3, and 0.5. The facet is at the right end.

in three dimensions along the waveguide, FEMLAB is capable of performing the integrations as defined in Eq. 5.2. All reflectivity values presented in this chapter use this method. Due to the memory limitations in the three-dimensional simulations, the calculated values for the standing-wave needed to be fitted to the analytical form in Eq. 5.2. Appendix C describes the fitting methods used.

5.3 Semi-Insulating Surface-Plasmon Resonators

As discussed in Section 3.3.3, previous analysis of SI surface-plasmon waveguides utilized the effective index method in calculating the mirror coupling loss. For a GaAs/Air interface, where $n_{\mathrm{GaAs}} = 3.6$, this gives a mirror reflectivity of $R = 0.3195$. Selected frequencies were simulated for the SI surface-plasmon waveguide and the results are shown in Table 5.1. The only waveguide parameter that changed for the frequencies were the respective plasma doping levels. As seen, numerical results for all frequencies tested are close enough to the 0.3195 to reaffirm the validity of the effective index method in calculating mirror reflectivities for the SI surface-plasmon waveguide.

Table 5.1: SI surface-plasmon facet reflectivities for 2–5 THz. All of the structures simulated have the following geometry: 0.4 μm top metal contact, 10 μm active region (doped at 2×10^{15} cm^{-3}), 0.5 μm plasma layer (doping listed), on a 100 μm substrate with a bottom metal coating.

SI Surface-Plasmon Waveguide Facet Reflectivities

Frequency (THz)	Reflectivity (%)	Plasma Layer Doping ($\times10^{18}$ cm^{-3})
2.0	28.95	1.0
2.5	32.48	1.0
3.0	32.14	1.0
4.0	31.08	2.0
5.0	30.39	3.0
6.0	30.02	4.5
7.0	29.66	5.0

Fig. 5-2 overlays radiation patterns for various frequencies of the SI surface-plasmon waveguide and show no major coupling effects with the bottom substrate surface-plasmon; the far-field pattern is similar to that predicted by Fourier optics.

5.4 Metal-Metal Resonators

The waveguide apertures for metal-metal structures are much less than the laser free-space wavelength and previous approximations used for reflection and transmission calculations of shorter wavelength structures fail to hold. The failures mainly come about because previous theories assumed incident and transmitted infinite-plane waves. However, coupling contributions between the components of the fields at the aperture's boundary become non-negligible for cases of subwavelength apertures. Specifically, as will be seen, output coupling with the surface plasmons associated with the metal aperture become important.

5.4.1 Reflectivity

Fig. 5-4 displays two-dimensional results of metal-metal facet reflectivities vs. frequency for different values of the active region thickness. The transition between microwave and optical waveguide design clearly falls in the THz regime (1-10 THz)

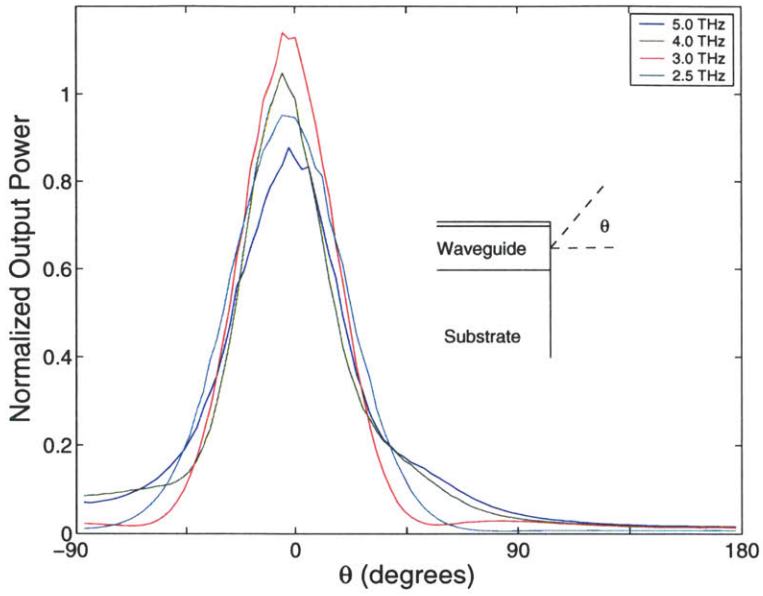

Figure 5-2: Normalized power radiation patterns for SI surface-plasmon waveguides for the respective frequencies listed in Table 5.1. The active region thickness is 10 μm thick, the plasma layer is 0.5 μm thick, and the substrate is 100 μm thick. The varied parameters are listed in Table 5.1.

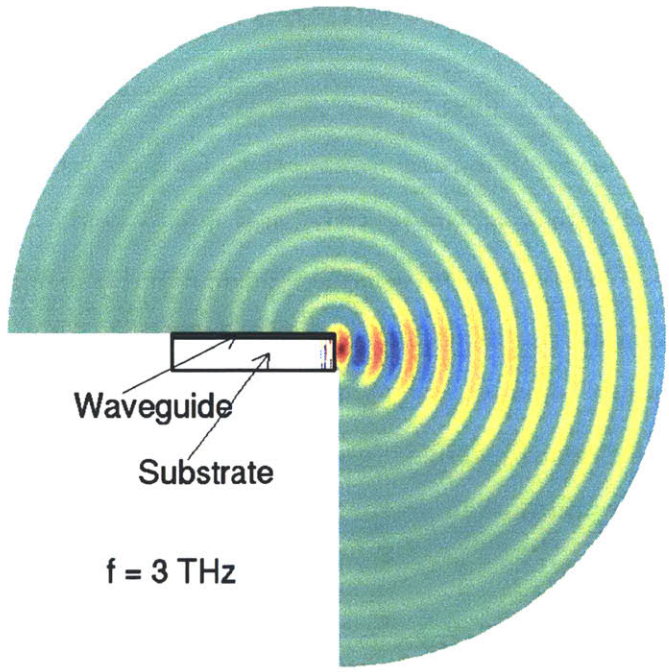

Figure 5-3: Field profile of the radiated transverse magnetic field for the SI surface-plasmon waveguide for the 3 THz case shown in Fig. 5-2.

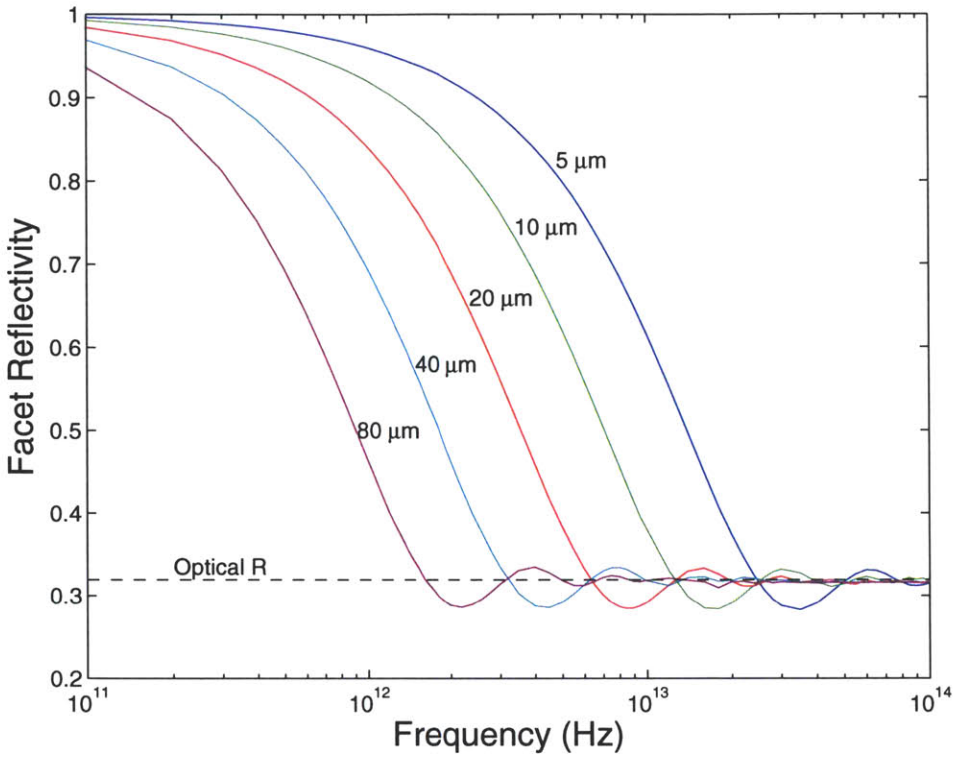

Figure 5-4: Two-dimensional (waveguide width is infinite) metal-metal waveguide facet reflectivities vs. frequency for five different waveguide thicknesses as labeled.

and a simple effective index method by itself would fail to account for these higher facet reflectivities. The oscillatory behavior as the reflectivity converges to the optical reflection value is interesting because it suggests an enhanced transmission of light in comparison with plane-wave transmission. This enhanced transmission appears to be due to surface-plasmon coupling effects on or near the metal aperture's boundary and is similar to results in studies done on near-field scanning optical microscopy [39, 40]. Coupling of the output power with surface plasmons at or near the metal aperture boundary can be seen in Figs. 5-6 and 5-7 and is discussed in the next section. Fig. 5-5 displays three-dimensional results of metal-metal facet reflectivities. The increase in reflectivity as the waveguide width decreases can be explained by the decrease in the area of the waveguide aperture; in the context of antenna theory, power radiated from subwavelength apertures are usually linearly proportional to the area of the aperture [37].

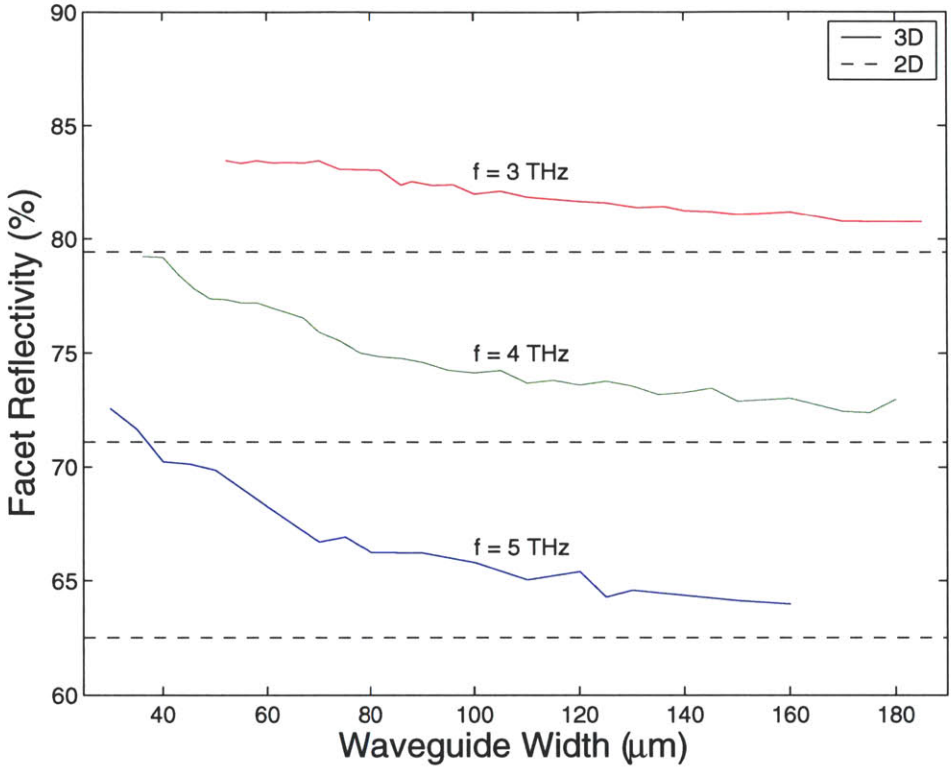

Figure 5-5: Three-dimensional metal-metal waveguide facet reflectivities vs. waveguide width for f = 3, 4, and 5 THz with a waveguide thickness set at 10 μm; overlaid are the two-dimensional values to show convergence.

5.4.2 Directivity

Fig. 5-6(a) overlays power directivity patterns for varying frequencies of a 10 μm thick metal-metal waveguide; Fig. 5-6(b) overlays power directivity patterns for varying thicknesses of the metal-metal waveguide at a frequency of 3 THz. Radiated field profiles for four cases of frequency (2, 6, 10, and 20 THz) with an active region thickness set at 10 μm are presented in Fig. 5-7. All were simulated in the two-dimensional mode solver in which the width of the waveguide is inherently infinite. The figures show that aperture boundary coupling to both the substrate surface plasmon and the top metal surface-plasmon (above the waveguide) drastically affect the directivity patterns. The former effectively radiates more power downward, while the latter effectively radiates power up and behind ($\theta > 90^o$) the waveguide with respect to the facet. It is seen that only a fraction of the coupled output power actually is radiated within a small enough angle to be collected by a cone.

5.5 Discussions

Two- and three-dimensional simulation results for SI surface-plasmon and metal-metal resonators in the THz regime have been presented. The effective index method is shown to stay valid in the THz regime for SI surface-plasmon resonators. Radiation patterns for SI surface-plasmon waveguides are similar to that predicted by Fourier optics. Metal-metal resonators, on the other hand, are seen to be a hybrid between the microwave and optical regimes. Two degrading factors arise in this intermediate regime: the facet reflectivity increases dramatically and the directivity of the output power decreases. The former factor is a major issue in trying to couple power out of the laser resonator. The later factor is a major issue in trying to couple the power that actually couples out of the resonator into some collection device, such as a cone, that efficiently directs the power toward a destination.

Current studies on second-order diffraction gratings as a DFB are being undertaken to address both of these issues for the metal-metal waveguide. Preliminary results are promising; they show that using the top metal contact as a grating not

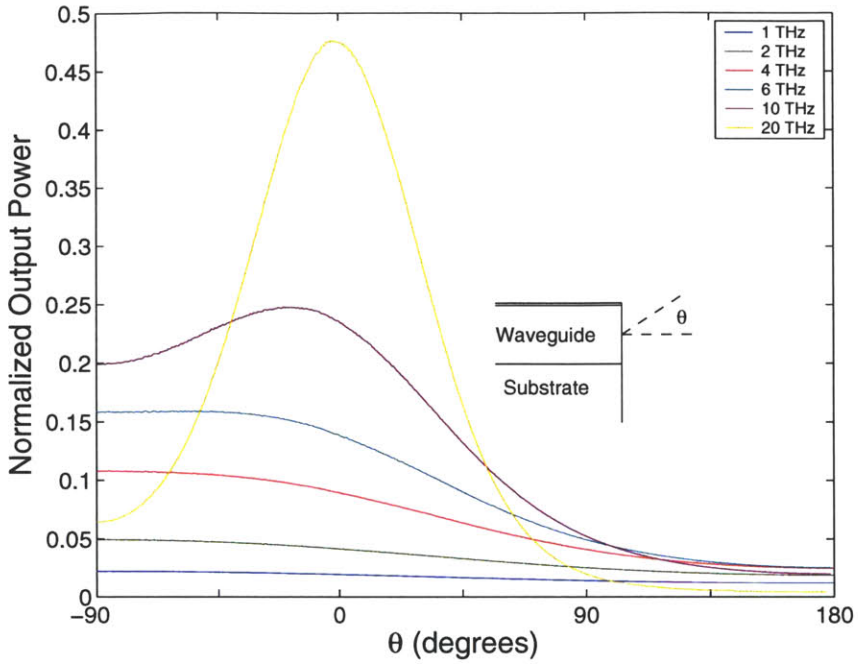

(a)

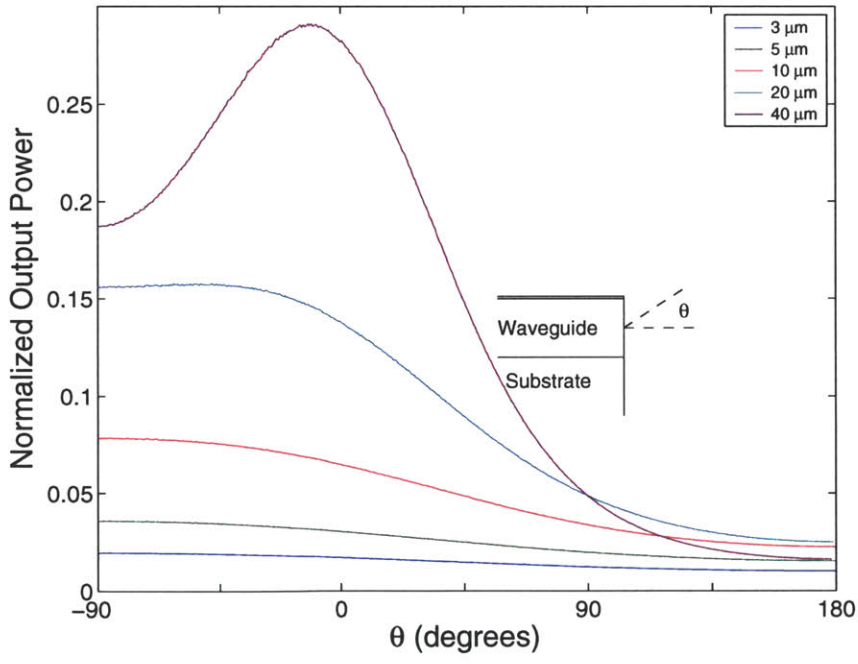

(b)

Figure 5-6: Normalized two-dimensional power radiation patterns for metal-metal waveguides; the power is normalized to the input power of the waveguide and thus includes varying facet reflectivities for each thickness and frequency. (a) Sets of power radiation patterns at different frequencies for a waveguide thickness of 10 μm. (b) Sets of power radiation patterns at different waveguide thicknesses for 3 THz.

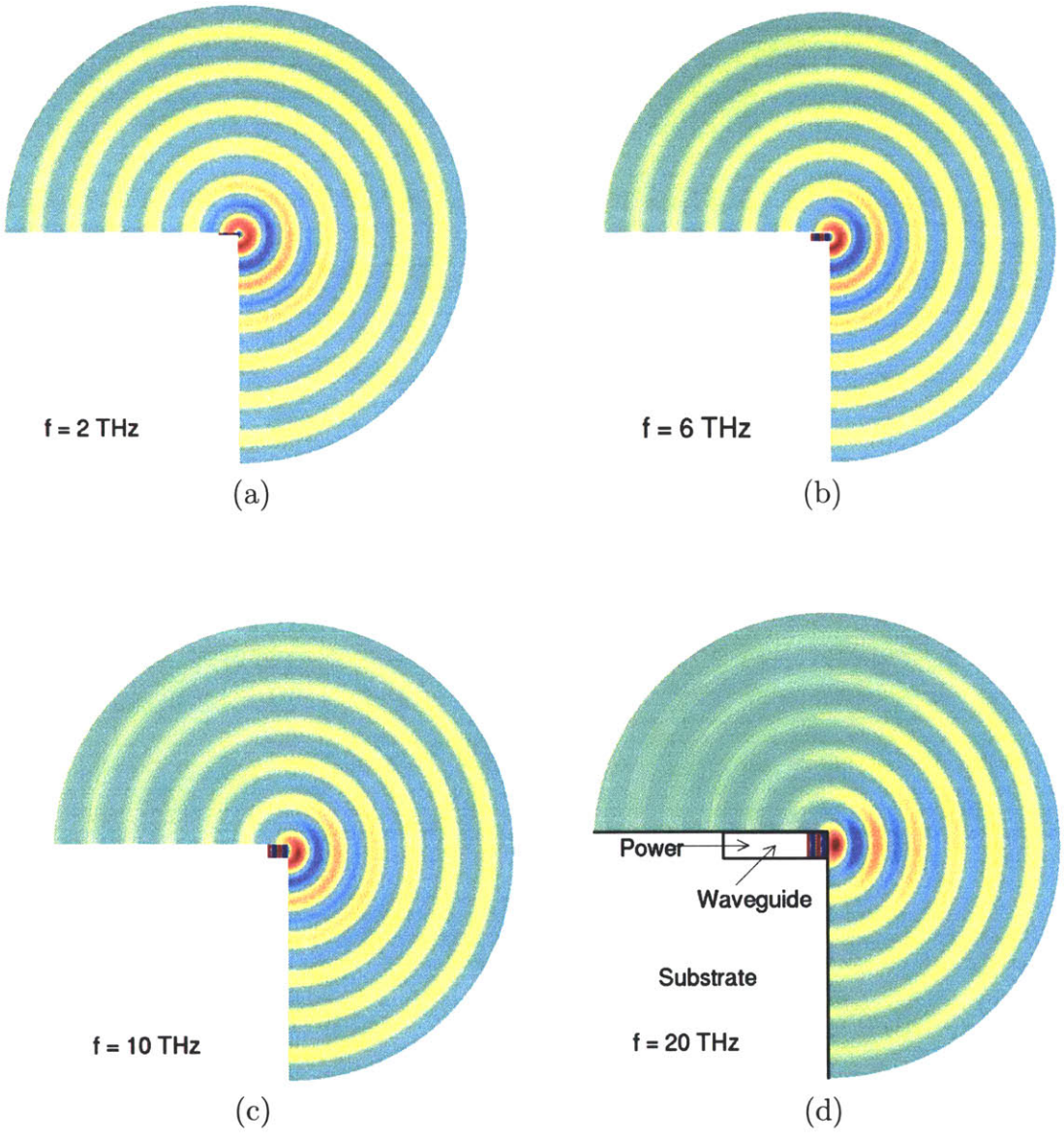

Figure 5-7: Field profiles of the radiated transverse magnetic field for the metal-metal waveguide at frequencies of (a) 2, (b) 6, (c) 10, and (d) 20 THz, from Fig. 5-6(a). The active region thickness for all cases is 10 μm.

only efficiently couples power out, but also provides higher directivity and symmetry of the radiation pattern, and may provide an effective tuning mechanism for the laser.

Appendix A

FEMLAB: Partial Differential Equations

FEMLAB is a powerful modeling tool based on the finite element method (FEM) for solving complicated partial differential equations (PDEs). Included in the FEMLAB package is an electromagnetics module with numerous pre-defined application modes that encompass electrostatic fields, magnetostatic fields, quasi-static fields, and electromagnetic waves in two- and three-dimensions. Beyond the graphical user interface, in which the user simply enters material and system parameters and presses the solve button, it is beneficial to examine how FEMLAB operates on a more fundamental level. Reasons for this might include the need to refine or modify specific parameters, such as a boundary condition coefficient, for a special situation not included in the pre-defined application mode, or, for post-processing purposes, a required knowledge of the application mode definitions, in this case in the context of electromagnetics. This appendix describes how FEMLAB formulates PDEs and the various types of analysis used in solving these PDEs.

FEMLAB formulates PDEs in three different ways: coefficient form, general form, and weak form. The latter, despite its name, is the most powerful and more general of the three. The general form is most suited for nonlinear problems. The coefficient form, which is what is used in the simulations discussed in this thesis, is most suited for linear problems and is the focus of what follows.

Once a PDE form is specified, various types of analysis are available and include: eigenfrequency and modal analysis, stationary and time-dependent analysis, and linear and nonlinear analysis. All simulations carried out in this thesis are linear and fall under either modal analysis, Chapter 4, or a stationary time-harmonic analysis, Chapter 5.

The FEMLAB coefficient formulation of PDEs on a geometry in n dimensions with one dependent variable is presented first as the simplest example and then the particular cases used in this thesis follow. In all cases, Ω represents the solution domain and $\partial\Omega$ represents its boundary, with $\mathbf{n}$ denoting the outward unit normal vector on $\partial\Omega$.

A.1 Coefficient Formulation

The simplest coefficient formulation assumes one dependent variable u in n dimensions. A stationary PDE problem in FEMLAB is formulated as follows

$$\nabla \cdot (-c\nabla u - \boldsymbol{\alpha} u + \boldsymbol{\gamma}) + \boldsymbol{\beta} \cdot \nabla u + au = f \quad \text{in} \quad \Omega, \tag{A.1}$$

$$\left.\begin{aligned} \mathbf{n} \cdot (c\nabla u + \boldsymbol{\alpha} u - \boldsymbol{\gamma}) + qu &= g - h^T \mu \\ hu &= r \end{aligned}\right\} \quad \text{on} \quad \partial\Omega, \tag{A.2}$$

where $\nabla = (\partial/\partial x_1, \ldots, \partial/\partial x_n)^T$, $\{a, f, g, q, r, \mu\}$ are scalars, $\{\boldsymbol{\alpha}, \boldsymbol{\beta}, \boldsymbol{\gamma}\}$ are $n \times 1$ vectors, and c, h are $n \times n$ matrices. Eqs. (A.2) are the generalized Neumann and the Dirichlet boundary conditions (BCs), respectively. This representation of the BCs is unconventional because it imposes both Neumann and Dirichlet BCs at the same time, also known as a mixed or Robin BC. The particular cases used for simulations in this thesis are not affected by this discrepancy since the coefficients are specifically chosen such that only one BC is imposed at a time. Refer to reference [29, pp. **3**-25-41] for more detail.

A.2 Electromagnetic PDE Formulation

The simulations presented in this thesis were carried out in three different application modes within the electromagnetics module: the two-dimensional perpendicular hybrid-mode waves application mode, the two-dimensional in-plane TM waves application mode, and the three-dimensional electromagnetic waves application mode. TE- and TM-mode solvers also exist in FEMLAB; however, due to the inherent nature of the inhomogeneity of the waveguides in interest, the solutions will be a hybrid between TE and TM modes, and the hybrid-mode solver must be used. The terms "perpendicular" and "in-plane" refer to the orientation of the wave vectors with respect to the two-dimensional plane in which the structure is define. The hybrid-mode solver was used to solve for the two-dimensional eigenmodes of waveguides while the two-dimensional in-plane TM and three-dimensional electromagnetic wave mode solvers were used to solve for the facet reflectivities of the waveguide and its radiation pattern. In each case, the governing PDEs are Maxwell's equations. The general FEMLAB formulation for these modes is the solution of the three dependent variables denoted by $\mathbf{u} = (u_x, u_y, u_z)^T$. The stationary PDE problem for these modes in FEMLAB is formulated as follows

$$\nabla \cdot (-c\nabla \mathbf{u}) + a\mathbf{u} = 0 \quad \text{in} \quad \Omega, \tag{A.3}$$

$$\left.\begin{aligned} \mathbf{n} \cdot (c\nabla \mathbf{u}) + q\mathbf{u} &= g \\ h\mathbf{u} &= 0 \end{aligned}\right\} \quad \text{on} \quad \partial\Omega, \tag{A.4}$$

A.2.1 Three-dimensional electromagnetic waves application mode

For the electromagnetic wave modes, FEMLAB treats time-harmonic waves with two formulations. FEMLAB uses the EE convention and assumes time dependence $\sim e^{i\omega t}$, in which case Maxwell's equations in homogeneous and isotropic subdomains can be

reduced to

$$\nabla \times (\nabla \times \mathbf{E}) - \omega^2 \mu \epsilon \mathbf{E} = \mathbf{0}, \tag{A.5}$$

$$\nabla \times (\nabla \times \mathbf{H}) - \omega^2 \mu \epsilon \mathbf{H} = \mathbf{0}. \tag{A.6}$$

Either of these equations may be used to solve Maxwell's equations, and FEMLAB assigns each as a different application mode. The simulations in this thesis dealt with hybrid-eigenmodes predominately TM in nature and thus used the latter magnetic field solver, Eq. (A.6). In this case, the coefficients for Eq. (A.3) are set to

$$a = -\omega^2 \mu_0 \mu_r \epsilon_0, \quad \text{and} \tag{A.7}$$

$$c = \frac{1}{\epsilon_r} \begin{bmatrix} \begin{bmatrix} 0 & 0 & 0 \\ 0 & 1 & 0 \\ 0 & 0 & 1 \end{bmatrix} & \begin{bmatrix} 0 & 0 & 0 \\ -1 & 0 & 0 \\ 0 & 0 & 0 \end{bmatrix} & \begin{bmatrix} 0 & 0 & 0 \\ 0 & 0 & 0 \\ -1 & 0 & 0 \end{bmatrix} \\ \begin{bmatrix} 0 & -1 & 0 \\ 0 & 0 & 0 \\ 0 & 0 & 0 \end{bmatrix} & \begin{bmatrix} 1 & 0 & 0 \\ 0 & 0 & 0 \\ 0 & 0 & 1 \end{bmatrix} & \begin{bmatrix} 0 & 0 & 0 \\ 0 & 0 & 0 \\ 0 & -1 & 0 \end{bmatrix} \\ \begin{bmatrix} 0 & 0 & -1 \\ 0 & 0 & 0 \\ 0 & 0 & 0 \end{bmatrix} & \begin{bmatrix} 0 & 0 & 0 \\ 0 & 0 & -1 \\ 0 & 0 & 0 \end{bmatrix} & \begin{bmatrix} 1 & 0 & 0 \\ 0 & 1 & 0 \\ 0 & 0 & 0 \end{bmatrix} \end{bmatrix}. \tag{A.8}$$

As is seen, the coefficient c is a rank-four tensor. See reference [44] for more interesting cases of anisotropic media. With these coefficients, $\mathbf{u} = \mathbf{H}$.

Boundary conditions

Only those boundary conditions used in the simulations of this thesis are discussed below; they are the perfect magnetic conductor (PMC) BC, the perfect electric conductor (PEC) BC, the matched BC, and the low-reflecting BC. Refer to [44, pp.

3-98-104] for a complete formulation of the electromagnetic waves application mode's boundary conditions, including the coefficients used in Eqs. (A.4).

The PMC condition $\mathbf{n}\times\mathbf{H} = \mathbf{0}$ sets the tangential component of the $\mathbf{H}$ field to zero. In modal analysis, Chapter 4, when a geometry is symmetric and the solution for a TM mode we are interested in is even, then the tangential magnetic field components (H_y and H_z) of the eigenmode are zero on the line of symmetry. This is illustrated in Fig. A-1. Therefore, the PMC condition can be used on the line of symmetry such that only one side of the geometry need be computed. This saves considerable memory that could otherwise be used to refine the mesh. If the solution is odd, see Fig. A-1, then the tangential electric field components (E_y and E_z) are zero on the line of symmetry and the PEC condition can be used.

The PEC condition $\mathbf{n} \times \mathbf{E} = \mathbf{0}$ sets the tangential component of the $\mathbf{E}$ field to zero. This is used for the metal boundaries of the waveguide if we are interested in the lossless case. This was also the preferred BC used in Ch. 4 at the outer boundaries; the fields should be negligible at this distance from the confined region and should not make a difference. The coefficients for Eq. (A.4) for the PMC and PEC cases are given under the Dirichlet BC as

$$h_{\mathrm{PMC}} = \begin{pmatrix} 0 & -n_z & n_y \\ n_z & 0 & -n_x \\ -n_y & n_x & 0 \end{pmatrix}, \qquad h_{\mathrm{PEC}} = 0, \tag{A.9}$$

where $\mathbf{n}$ is outward unit normal vector.

Two absorbing boundary conditions are available to represent non-physical boundaries: the matched BC and the low-reflecting BC. The matched BC (for three dimensions) is given by

$$\mathbf{n} \times (\nabla \times \mathbf{E}) - i\beta(\mathbf{E} - (\mathbf{n} \cdot \mathbf{E})\mathbf{n}) = -2i\beta(\mathbf{E}_0 - (\mathbf{n} \cdot \mathbf{E}_0)\mathbf{n}) - 2i\beta\sqrt{\frac{\mu_0}{\epsilon}}\mathbf{n} \times \mathbf{H}_0, \tag{A.10}$$

where $\mathbf{E}_0$ and $\mathbf{H}_0$ are optional input parameters and β is a given propagation constant. The derivation of Eq. A.10 is beyond the scope of this section; however, it can readily

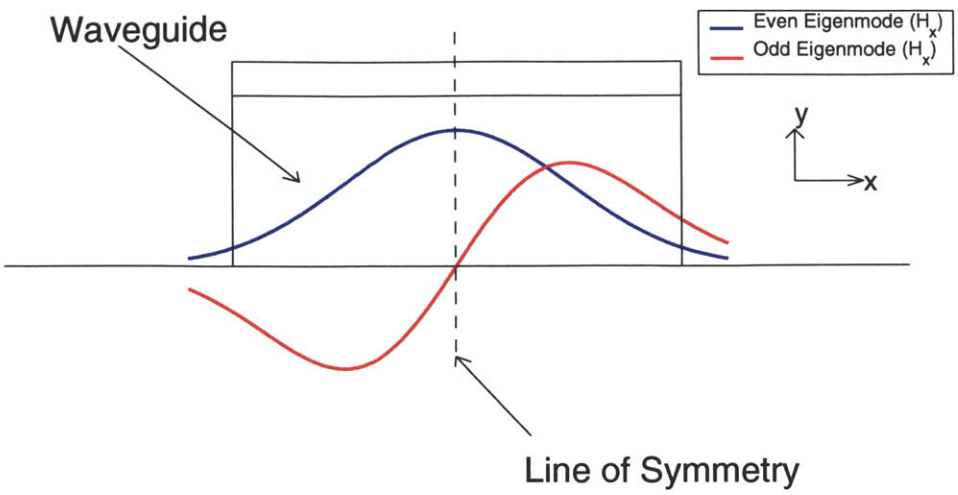

Figure A-1: H_x field profiles for odd and even eigenmodes for symmetric waveguides.

be verified[1] that in the case that no sources are present, Eq. A.10 becomes

$$\mathbf{n} \times (\nabla \times \mathbf{E}) - i\beta(\mathbf{E} - (\mathbf{n} \cdot \mathbf{E})\mathbf{n}) = 0,$$

and this condition is satisfied by a plane wave $\mathbf{E} = \hat{\mathbf{E}} e^{-i\beta \mathbf{n} \cdot \mathbf{r}}$ traveling out through the boundary. Inclusion of the source terms are described in Ref. [44, pp. 3-100-101]

The matched BC, Eq. A.10, is used to perfectly absorb an incident eigenmode with propagation constant β. In this thesis, the matched BC was used in facet reflectivity calculations at the input to the waveguide; the fundamental eigenmode of the waveguide was used as an input and any reflections of this eigenmode would be perfectly absorbed. The matched BC also effectively absorbs higher order mode waves depending on how close their propagation constants are to β, which in most cases are close enough to consider the higher order modes perfectly absorbed as well. In the case the propagation constants differ, the error is mitigated by the fact that the higher mode usually carries less power associated with the lower propagation constant.

The low-reflecting BC is a special case of the matched BC by setting the propagation constant to be that of free space: $\beta = k = \omega\sqrt{\mu\epsilon}$. FEMLAB implements the

[1]Using the equality: $\mathbf{n} \times (\mathbf{n} \times \mathbf{E}) = (\mathbf{n} \cdot \mathbf{E})\mathbf{n} - \mathbf{E}$.

low-reflecting BC as

$$\sqrt{\frac{\mu_0}{\epsilon_0}}\mathbf{n}\times\mathbf{H}+\mathbf{E}-(\mathbf{n}\cdot\mathbf{E})\mathbf{n}=2\mathbf{E}_0-2(\mathbf{n}\cdot\mathbf{E}_0)\mathbf{n}+2\sqrt{\frac{\mu_0}{\epsilon_0}}\mathbf{n}\times\mathbf{H}_0,$$

where, again, $\mathbf{E}_0$ and $\mathbf{H}_0$ are optional input parameters. In the case that no sources are present, this becomes

$$\sqrt{\frac{\mu_0}{\epsilon_0}}\mathbf{n}\times\mathbf{H}=(\mathbf{n}\cdot\mathbf{E})\mathbf{n}-\mathbf{E}=\mathbf{n}\times(\mathbf{n}\times\mathbf{E}).$$

The low-reflecting BC is perfectly absorbing for infinite plane waves, as verified by inserting a free-space plane wave $\hat{\mathbf{E}}e^{-i\beta_0\mathbf{n}\cdot\mathbf{r}}$ into the above equation. In this thesis, the low-reflecting BC was used at the outer boundaries in the facet reflectivity calculations. The distance was made to be a minimum number of wavelengths such that the fields are radiating waves (in the Fraunhofer or radiating far-field region) and are approximately absorbed as infinite plane waves.

The coefficients for the absorbing boundary conditions in two and three dimensions are given in Ref. [44].

A.2.2 Two-dimensional in-plane TM waves

For the two-dimensional in-plane TM wave mode [2], the fields can be written as:

$$\mathbf{H}(x,y,t)=\hat{\mathbf{z}}H_z(x,y)e^{i(\omega t-\beta_x x-\beta_y y)} \tag{A.11}$$

$$\mathbf{E}(x,y,t)=\left(\hat{\mathbf{x}}E_x(x,y)+\hat{\mathbf{y}}E_y(x,y)\right)e^{i(\omega t-\beta_x x-\beta_y y)}, \tag{A.12}$$

where it is explicit that the wave vector, $\boldsymbol{\beta}=\hat{\mathbf{x}}\beta_x+\hat{\mathbf{y}}\beta_y$, is in the x-y plane. Eq. A.3 becomes

$$-\nabla\cdot(\epsilon_r\nabla H_z)-k_0^2H_z=0. \tag{A.13}$$

[2]For two-dimensional simulations, the axes are oriented such that the x-axis is horizontal on the screen, the y-axis is vertical, and the z-axis is pointing out of the screen

A.2.3 Two-dimensional perpendicular hybrid-mode waves

For the two-dimensional perpendicular hybrid-mode, the fields can be written as:

$$\mathbf{H}(x,y,z,t) = \mathbf{H}(x,y)e^{i(\omega t-\beta z)} \tag{A.14}$$

$$\mathbf{E}(x,y,z,t) = \mathbf{E}(x,y)e^{i(\omega t-\beta z)}. \tag{A.15}$$

Eq. A.3 becomes

$$\nabla \times (\epsilon_r^{-1}\nabla \times \mathbf{H}) - k_0^2\mu_r\mathbf{H} = \mathbf{0}. \tag{A.16}$$

Appendix B

Surface Plasmons

Conventional dielectric waveguides provide confinement by small refractive-index differences between layers. This method is impractical for THz QCLs. However, Maxwell's equations allow another mechanism for confinement between two layers provided that the dielectric constants of the two materials have real parts of opposite sign. These modes are known as surface plasmons and can propagate along the interface of the two layers. The simplest two-layer surface plasmon is analytically described for three cases in this appendix. The first is a simple metal/vacuum surface plasmon for comparison. The next two are the separate solutions for the Au/GaAs active region surface plasmon and the GaAs plasma layer/GaAs active region surface plasmon.

Let us assume, quite arbitrarily for now, that the half-space (labeled 2) $z < 0$ has a permittivity $\epsilon_2 = \epsilon_2(\omega)$, and that the half-space $z > 0$ (labeled 1) has a permittivity

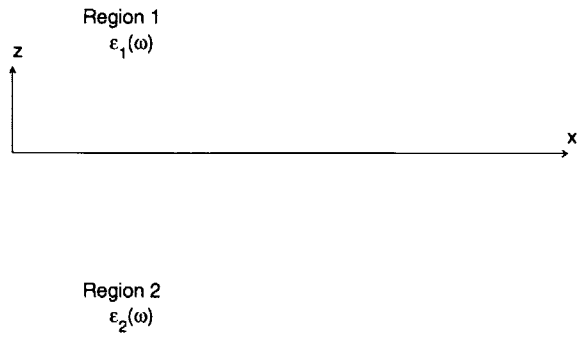

Figure B-1: Surface plasmon coordinates.

$\epsilon_1 = \epsilon_1(\omega)$ (see Fig. B-1). The surface plasmon is a solution to Maxwell's equations of the form (see problem 1.5 in Ref. [31]):

$$\mathbf{E}_1(z>0) = \frac{1}{\sqrt{\alpha_1^2+k_x^2}}(\hat{\mathbf{x}}\alpha_1 + \hat{\mathbf{z}}ik_x)\,e^{ik_x x}e^{-\alpha_1 z} \tag{B.1}$$

and

$$\mathbf{E}_2(z<0) = \frac{1}{\sqrt{\alpha_2^2+k_x^2}}(\hat{\mathbf{x}}\alpha_2 - \hat{\mathbf{z}}ik_x)\,e^{ik_x x}e^{\alpha_2 z} \tag{B.2}$$

where k_x, α_1, and α_2 may be complex and are found to be:

$$\alpha_1(\omega) = \omega\sqrt{-\mu_0\frac{\epsilon_1^2}{\epsilon_1+\epsilon_2}}, \tag{B.3}$$

$$\alpha_2(\omega) = -\omega\sqrt{-\mu_0\frac{\epsilon_2^2}{\epsilon_1+\epsilon_2}}, \tag{B.4}$$

$$k_x(\omega) = \omega\sqrt{\mu_0\frac{\epsilon_1\epsilon_2}{\epsilon_1+\epsilon_2}}. \tag{B.5}$$

B.1 Metal/Vacuum Surface Plasmon

The simplest surface plasmon mode exists between a metal with $\epsilon_1(\omega) = \epsilon_0(1-\omega_p^2/\omega^2)$ and a vacuum with $\epsilon_2(\omega) = \epsilon_0$. The propagation constant of the surface plasmon becomes:

$$k_x(\omega) = \frac{\omega}{c}\sqrt{\frac{\omega_p^2-\omega^2}{\omega_p^2-2\omega^2}}. \tag{B.6}$$

The surface plasmon is seen to be propagating (having a real k_x) for $\omega > \omega_p$ and $\omega < \omega_p/\sqrt{2}$, where $\omega_p/\sqrt{2}$ defines the surface plasmon frequency. Parameters for the metal/vacuum surface plasmon are plotted in Fig. B-2. The surface plasmon mode is seen to be only confined to the surface for $\omega < \omega_p/\sqrt{2}$.

B.2 Au/GaAs Active Region Surface Plasmon

The surface plasmon associated with the lightly doped GaAs active region and Au (present in both the SI surface-plasmon and metal-metal waveguides) is presented

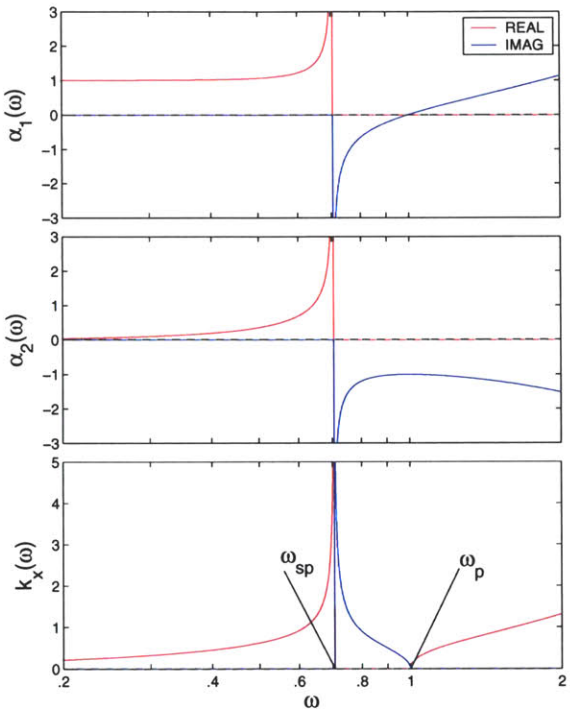

Figure B-2: $\alpha_1(\omega)$, $\alpha_2(\omega)$, and $k_x(\omega)$ values for the metal/vacuum surface plasmon vs. frequency. x-axis values are in units of ω_p and y-axis values are in units of ω_p/c.

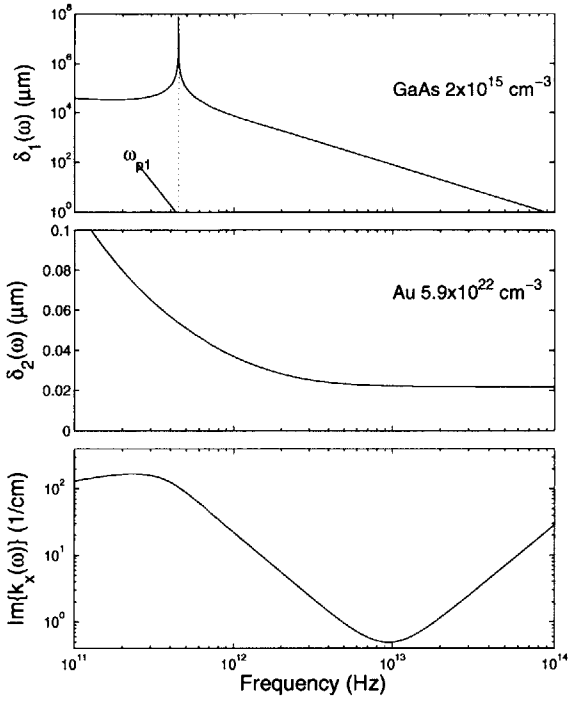

Figure B-3: Surface plasmon skin depths, δ_1 and δ_2, for GaAs doped at 2×10^{15} cm^{-3} and Au, respectively, and the attenuation constant are plotted. The GaAs bulk plasma frequency is denoted by ω_{p1} and is 430 GHz; the Au bulk plasma frequency is 2181 THz.

in Fig. B-3 using the Drude permittivity defined in Eq. 3.11 and the values in Table 3.1. The metal skin depth, given by $1/\mathrm{Im}\{|\alpha|\}$, is seen to increase with decreasing frequency until the frequency reaches the bulk plasma frequency of the GaAs active region, which is 430 GHz, well below the THz regime (1-10THz).

B.3 GaAs Active Region/GaAs Plasma Layer Surface Plasmon

The surface plasmon associated with the lightly doped GaAs active region and the n+ GaAs plasma layer (present in the SI surface-plasmon waveguide) is presented in Fig. B-4 using the Drude permittivity defined in Eq. 3.11 and the values in Table 3.1. The plasma skin depth is seen to be greater than those thicknesses used for the plasma layer in this thesis.

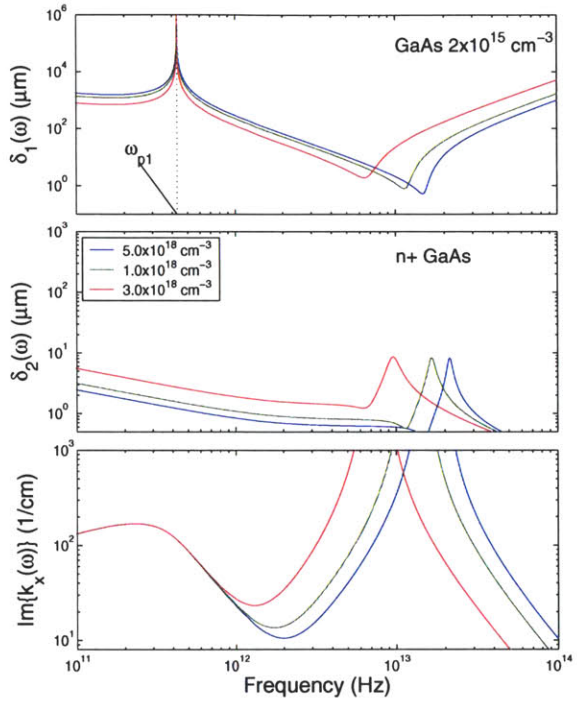

Figure B-4: Surface plasmon skin depths, δ_1 and δ_2, for GaAs doped at 2×10^{15} cm^{-3} and for three sets of n+ GaAs doped at 1, 3, and 5×10^{18} cm^{-3}, respectively, and the attenuation constant are plotted. The lightly doped GaAs bulk plasma frequency is denoted by ω_{p1} and is 430 GHz; the bulk plasma frequencies of the n+ GaAs are 9.64, 16.7, and 21.5 THz for the 1, 3, and 5×10^{18} cm^{-3} layers, respectively.

Appendix C

Standing-Wave Ratio Fitting

The SWR method is used in the calculation of facet reflectivities (see Chapter 5). By defining appropriate lines or planes, depending on the number of dimensions, of integration along the waveguide, FEMLAB is capable of performing the integrations as defined in Eq. 5.2. However, due to memory limitations, only a finite number of lines or planes may be defined and integrated. In three dimensions especially, memory limitations are severe enough such that no more then ten planes are usually defined along the waveguide, where the length is on the order of a wavelength. The accuracy of the SWR method rests on knowing the maximum and minimum field values of the standing-wave, Eq. 5.2. The maximum and minimum values obtained from the finite set of integration planes may differ enough from the true maximum and minimum values to skew the accuracy of the calculated reflectivity. However, due to the simple form of the standing-wave, the finite number of calculated values can accurately be fitted to the analytical form of the profile. From Eq. 5.2, the analytical form of the standing-wave is

$$|\langle \mathbf{h}(x,y)|\mathbf{H}(x,y,z)\rangle| = |1 + re^{-i\phi}e^{-i2\beta z}| = \sqrt{1 + r^2 + 2r\cos(\phi + 2\beta z)}, \qquad \text{(C.1)}$$

where the phase of the reflection coefficient, ϕ, is explicitly written. Newton's method along with the least squares method can be employed to fit the finite set of calculated values to this equation; this scheme is presented in this appendix and returns an

accurate value for the reflection coefficient.

C.1 SWR Fitting: Newton's Method and Least Squares

Define a residual function as follows:

$$\bar{\mathbf{f}}(A,r,\phi) \equiv A^2 \begin{pmatrix} 1+r^2+2r\cos(\phi+2\beta z_1) \\ 1+r^2+2r\cos(\phi+2\beta z_2) \\ \vdots \\ 1+r^2+2r\cos(\phi+2\beta z_N) \end{pmatrix} - \begin{pmatrix} d_1^2 \\ d_2^2 \\ \vdots \\ d_N^2 \end{pmatrix},$$

where β is the known propagation constant, and d_i are the calculated values of Eq. C.1 at the z_i locations. A, r, and ϕ are the unknowns to be determined.

The Jacobian matrix, $\bar{\bar{\mathbf{J}}}$, is defined by

$$\bar{\bar{\mathbf{J}}} \equiv \begin{pmatrix} \frac{\partial f_1}{\partial A} & \frac{\partial f_1}{\partial r} & \frac{\partial f_1}{\partial \phi} \\ \frac{\partial f_2}{\partial A} & \frac{\partial f_2}{\partial r} & \frac{\partial f_2}{\partial \phi} \\ \vdots & \vdots & \vdots \\ \frac{\partial f_N}{\partial A} & \frac{\partial f_N}{\partial r} & \frac{\partial f_N}{\partial \phi} \end{pmatrix}, \quad \text{where} \quad \begin{aligned} \frac{\partial f_i}{\partial A} &= 2A\left(1+r^2+2r\cos(\phi+2\beta z_i)\right), \\ \frac{\partial f_i}{\partial r} &= A^2\left(2r+2\cos(\phi+2\beta z_i)\right), \\ \frac{\partial f_i}{\partial \phi} &= -2rA^2\sin(\phi+2\beta z_i). \end{aligned}$$

C.1.1 Newton's method

A Taylor series around (A', r', ϕ') gives

$$\bar{\mathbf{f}}(A,r,\phi) = \bar{\mathbf{f}}(A',r',\phi') + \bar{\bar{\mathbf{J}}}\bar{\Delta} + O(\Delta^2), \quad \text{where} \quad \bar{\Delta} \equiv \begin{pmatrix} A-A' \\ r-r' \\ \phi-\phi' \end{pmatrix}.$$

Newton's method gives

$$\bar{\bar{\mathbf{J}}}\bar{\Delta} = -\bar{\mathbf{f}}(A',r',\phi'). \tag{C.2}$$

C.1.2 Least squares method

Eq. C.2 is an overdetermined system. The least squares method gives the best fit solution

$$\bar{\Delta} = -\left(\bar{\bar{\mathbf{J}}}^T \bar{\bar{\mathbf{J}}}\right)^{-1} \bar{\bar{\mathbf{J}}}^T \bar{\mathbf{f}}(A', r', \phi').$$

The iterative method employed is then

$$\begin{pmatrix} A_{m+1} \\ r_{m+1} \\ \phi_{m+1} \end{pmatrix} = \begin{pmatrix} A_m \\ r_m \\ \phi_m \end{pmatrix} - \left(\bar{\bar{\mathbf{J}}}_m^T \bar{\bar{\mathbf{J}}}_m\right)^{-1} \bar{\bar{\mathbf{J}}}_m^T \bar{\mathbf{f}}(A_m, r_m, \phi_m),$$

where the initial guess is

$$\begin{pmatrix} A_0 \\ r_0 \\ \phi_0 \end{pmatrix} = \begin{pmatrix} \sqrt{\dfrac{d_{\max}^2 + d_{\min}^2}{2}} \sqrt{\dfrac{1}{1+r_0^2}} \\ \dfrac{d_{\max} - d_{\min}}{d_{\max} + d_{\min}} \\ \cos^{-1}\left(\left(\dfrac{d_1^2}{A_0^2} - 1 - r_0^2\right)\dfrac{1}{2r_0}\right) \end{pmatrix}.$$

Fig. C-1 shows a typical example in which the finite number of lines (or planes) of integration inaccurately calculate the reflectivity value, in this case by 18%. Fitting the SWR by the above method reproduces more accurate minimum and maximum SWR values as seen.

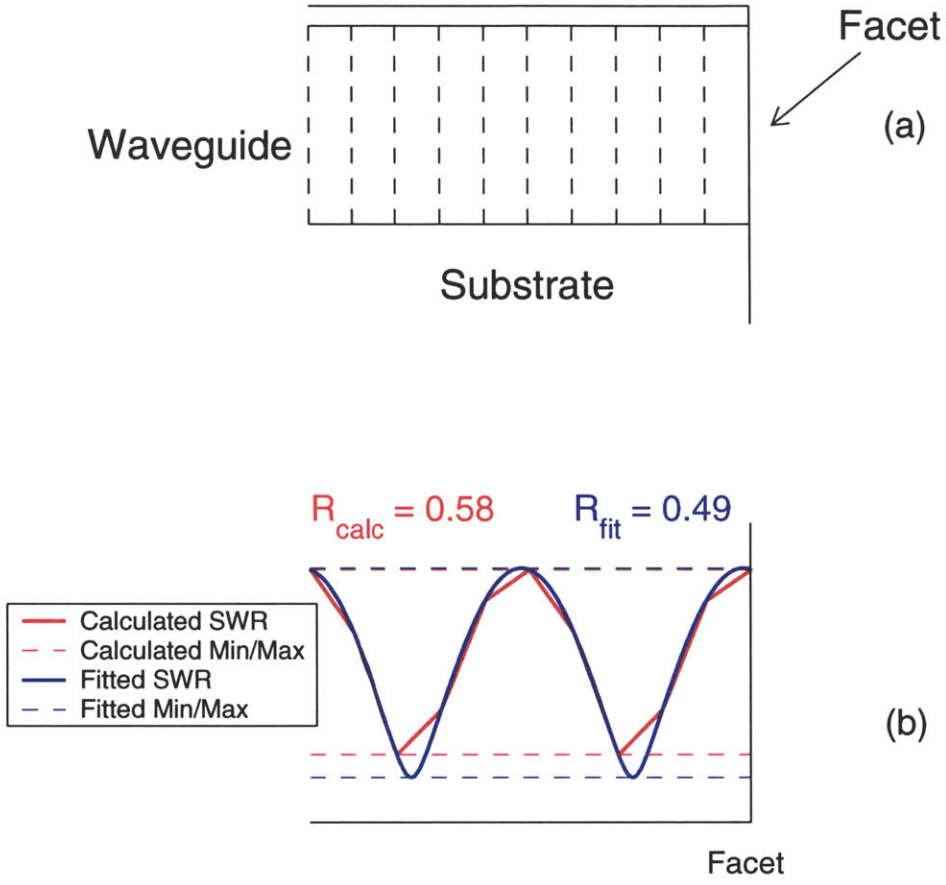

Figure C-1: SWR fitting example: (a) representative geometry of the waveguide; dashed lines are the defined lines of integration. (b) Calculated values at each line of integration are superimposed on the fitted SWR profile. It is seen that the calculated values over- and under-estimate the minimum and maximum SWR values, respectively. The calculated reflectivity value, R_{calc}, differs by 18% from the fitted value, R_{fit}.

Bibliography

[1] R. Köhler, A. Tredicucci, F. Beltram, H. E. Beere, E. H. Linfield, A. G. Davies, D. A. Ritchie, R. C. Iotti, and F. Rossi. Terahertz semiconductor-heterostructure laser. *Nature*, 417:156–159, 2002.

[2] M. Rochat, L. Ajili, H. Willenberg, J. Faist, H. Beere, G. Davies, E. Linfield, and D. Ritchie. Low-threshold terahertz quantum-cascade lasers. *Appl. Phys. Lett.*, 81:1381–1383, 2002.

[3] B. S. Williams, H. Callebaut, S. Kumar, Q. Hu, and J. L. Reno. 3.4-THz quantum cascade laser based on longitudinal-optical-phonon scattering for depopulation. *Appl. Phys. Lett.*, 82:1015–1017, 2003.

[4] R. Köhler, A. Tredicucci, F. Beltram, H. E. Beere, E. H. Linfield, A. G. Davies, D. A. Ritchie, S. S. Dhillon, and C. Sirtori. High-performance continuous-wave operation of superlattice terahertz quantum-cascade lasers. *Appl. Phys. Lett.*, 82:1518–1520, 2003.

[5] G. Scalari, L. Ajili, J. Faist, H. Beere, E. Linfield, D. Ritchie, and G. Davies. Far-infrared ($\lambda \approx 87\ \mu$m) bound-to-continuum quantum-cascade lasers operating up to 90 K. *Appl. Phys. Lett.*, 82:3165–3167, 2003.

[6] S. Kumar, B. S. Williams, S. Kohen, Q. Hu, and J. L. Reno. Continuous-wave operation of terahertz quantum-cascade lasers above liquid-nitrogen temperature. *Appl. Phys. Lett.*, 84:2494–2496, 2004.

[7] M. Helm, E. Colas, P. England, F. DeRosa, and Jr. S. J. Allen. Observation of grating-induced intersubband emission from GaAs/AlGaAs superlattice. *Appl. Phys. Lett.*, 53:1714–1716, 1988.

[8] J. Faist, F. Capasso, D. L. Sivco, C. Sirtori, A. L. Hutchinson, and A. Y. Cho. Quantum cascade laser. *Science*, 264:553–556, 1994.

[9] C. Sirtori, C. Gmachl, F. Capasso, J. Faist, D. L. Sivco, A. L. Hutchinson, and A. Y. Cho. Long wavelength infrared ($\lambda \approx 8$–11.5 μm) semiconductor lasers with waveguides based on surface plasmons. *Optics Lett.*, 23:1366–1368, 1998.

[10] C. Sirtori, J. Faist, F. Capasso, D. L. Sivco, A. L. Hutchinson, and A. Y. Cho. Quantum cascade laser with plasmon-enhanced waveguide operating at 8.4 μm wavelength. *Appl. Phys. Lett.*, 66:3242–3244, 1995.

[11] C. Sirtori, J. Faist, F. Capasso, D. L. Sivco, A. L. Hutchinson, and A. Y. Cho. Long wavelength infrared ($\lambda \approx 11$ μm) quantum cascade lasers. *Appl. Phys. Lett.*, 69:2810–2812, 1996.

[12] A. Tredicucci, C. Gmachl, F. Capasso, A. L. Hutchinson, D. L. Sivco, and A. Y. Cho. Single-mode surface-plasmon laser. *Appl. Phys. Lett.*, 76:2164–2166, 2000.

[13] A. Tredicucci, C. Gmachl, M. C. Wanke, F. Capasso, A. L. Hutchinson, D. L. Sivco, S. G. Chu, and A. Y. Cho. Surface plasmon quantum cascade lasers at $\lambda \approx 19$ μm. *Appl. Phys. Lett.*, 77:2286–2288, 2000.

[14] R. Colombelli, F. Capasso, C. Gmachl, A. L. Hutchinson, D. L. Sivco, A. Tredicucci, M. C. Wanke, A. M. Sergent, and A. Y. Cho. Far-infrared surface-plasmon quantum-cascade lasers at 21.5 μm and 24 μm wavelengths. *Appl. Phys. Lett.*, 78:2620–2622, 2001.

[15] K. Unterrainer, R. Colombelli, C. Gmachl, F. Capasso, H. Y. Hwang, A. M. Sergent, D. L. Sivco, and A. Y. Cho. Quantum cascade lasers with double metal-semiconductor waveguide resonators. *Appl. Phys. Lett.*, 80:3060–3062, 2002.

[16] B. Xu. *Development of Intersubband Terahertz Lasers Using Multiple Quantum Well Structures.* Ph.D. thesis, Massachusetts Institute of Technology, Department of Electrical Engineering and Computer Science, 1998.

[17] B. S. Williams, S. Kumar, H. Callebaut, Q. Hu, and J. L. Reno. Terahertz quantum-cascade laser at $\lambda \approx 100$ μm using metal waveguide for mode confinement. *Appl. Phys. Lett.*, 83:2124–2126, 2003.

[18] B. S. Williams. *GaAs/AlGaAs Mid-Infrared Quantum Cascade Laser.* M.S. thesis, Massachusetts Institute of Technology, Department of Electrical Engineering and Computer Science, 1998.

[19] L. Ajili, G. Scalari, D. Hofstetter, M. Beck, J. Faist, H. Beere, G. Davies, E. Linfield, and D. Ritchie. Continuous-wave operation of far-infrared quantum cascade lasers. *Electron. Lett.*, 38:1675–1676, 2002.

[20] B. S. Williams. *Terahertz quantum dascade lasers.* Ph.D. thesis, Massachusetts Institute of Technology, Department of Electrical Engineering and Computer Science, 2003.

[21] S. Barbieri, J. Alton, M. Evans, S. S. Dhillon, H. E. Beere, E. H. Linfield, A. G. Davies, D. A. Ritchie, R. Köhler, A. Tredicucci, and F. Beltram. Continuous wave terahertz quantum cascade laser. In *IEEE Tenth International Conference on Terahertz Electronics Proceedings*, pages 105–108, 2002.

[22] S. L. Chuang. *Physics of Optoelectronic Devices.* Wiley Series in Pure and Applied Optics. John Wiley and Sons, New York, 1995.

[23] J. Ulrich, R. Zobl, N. Finger, K Unterrainer, G. Strasser, and E. Gornik. Terahertz-electroluminescence in a quantum cascade structure. *Physica B*, 272:216–218, 1999.

[24] R. Courant. Variational methods for the solution of problems of equilibrium and vibrations. *Bull. Am. Math. Soc.*, 49:1–23, 1943.

[25] K. H. Huebner, D. L. Dewhirst, D. E. Smith, and T. G. Byrom. *The Finite Element Method for Engineers.* John Wiley and Sons, New York, fourth edition, 2001.

[26] J. Jin. *The Finite Element Method in Electromagnetics.* John Wiley and Sons, New York, second edition, 2002.

[27] M. N. O. Sadiku. *Numerical Techniques in Electromagnetics.* CRC Press, Boca Raton, FL, second edition, 2001.

[28] G. Strang and G. J. Fix. *An Analysis of the Finite Element Method.* Prentice-Hall Series in Automatic Computation. Prentice Hall, Englewood Cliffs, NJ, 1973.

[29] COMSOL AB, Burlington, MA. *FEMLAB: Reference Manual,* second printing edition, November 2001.

[30] N. N. Rao. *Elements of Engineering Electromagnetics.* Prentice Hall, Upper Saddle River, NJ, fifth edition, 2000.

[31] N. W. Ashcroft and N. D. Mermin. *Solid State Physics.* Harcourt Brace College Publishing, Fort Worth, 1976.

[32] P. G. Huggard, J. A. Cluff, G. P. Moore, C. J. Shaw, S. R. Andrews, S. R. Keiding, E. H. Linfield, and D. A. Ritchie. Drude conductivity of highly doped GaAs at terahertz frequencies. *J. Appl. Phys.*, 87:2382–2385, 2000.

[33] V. W. L. Chin, T. Osotchan, M. R. Vaughan, T. L. Tansley, G. J. Griffiths, and Z. Kachwalla. Hall and drift mobilities in molecular beam epitaxial grown GaAs. *J. Elec. Mat.*, 22:1317, 1993.

[34] M. A. Ordal, L. L. Long, R. J. Bell, S. E. Bell, R. R. Bell, Jr. R. W. Alexander, and C. A. Ward. Optical properties of the metals Al, Co, Cu, Au, Fe, Pb, Ni, Pd, Pt, Ag, Ti, and W in the infrared and far infrared. *Appl. Optics*, 22:1099–1120, 1983.

[35] W. J. Moore and R. T. Holm. Infrared dielectric constant of gallium arsenide. *J. Appl. Phys.*, 80:6939–6942, 1996.

[36] R. E. Collin. *Foundations for Microwave Engineering.* IEEE Press Series on Electromagnetic Wave Theory. IEEE Press, New York, second edition, 2001.

[37] R. E. Collin. *Antennas and Radiowave Propagation.* McGraw-Hill Series in Electrical Engineering. McGraw-Hill, Inc., 1985.

[38] H. A. Bethe. Theory of diffraction by small holes. *Phys. Rev.*, 66:163–182, 1944.

[39] H. J. Lezec, A. Degiron, E. Devaux, R. A. Linke, L. Martin-Moreno, F. J. Garcia-Vidal, and T. W. Ebbesen. Beaming light from a subwavelength aperture. *Science*, 297:820–822, 2002.

[40] D. J. Shin, A. Chavez-Pirson, S. H. Kim, S. T. Jung, and Y. H. Lee. Diffraction by a subwavelength-sized aperture in a metal plane. *J. Opt. Soc. Am. A*, 18:1477–1486, 2001.

[41] M. J. Lockyear, A. P. Hibbins, J. R. Sambles, and C. R. Lawrence. Surface-topography-induced enhanced transmission and directivity of microwave radiation through a subwavelength circular metal aperture. *Appl. Phys. Lett.*, 84:2040–2042, 2004.

[42] H. Kogelnik. Theory of optical waveguides. In T. Tamir, editor, *Guided-Wave Optoelectronics*, number 26 in Springer Series in Electronics and Photonics, chapter 2, pages 7–87. Springer-Verlag, Berlin, second edition, 1990.

[43] D. Indjin, Z. Ikonić, P. Harrison, and R. W. Kelsall. Surface plasmon waveguides with gradually doped or NiAl intermetallic compound buried contact for terahertz quantum cascade lasers. *J. Appl. Phys.*, 94:3249–3252, 2003.

[44] COMSOL AB, Burlington, MA. *FEMLAB: Electromagnetics Module*, third printing edition, June 2002.